ACS EARTH AND SPACE CHEMISTRY

http://pubs.acs.org/journal/aesccq Article

Threshold Calibration of Redox Conditions in Lacustrine Fine-Grained Sedimentary Rocks Based on the Internal Cross-Calibration of Multiple Redox Proxies: A Case Study of the Upper Triassic Chang 8–Chang 7 Members in the Southern Ordos Basin, China

Huimin Zhang, Zhihuan Zhang,* Dongdong Xia, Ruihui Zheng, Lei Cao, Qing Li, and Hao Lu

Cite This: *ACS Earth Space Chem.* 2023, 7, 120–141 **Read Online**

ABSTRACT: Redox conditions of lacustrine strata assessed by redox proxies with unified thresholds were conflicted in the Ordos Basin. The internal cross-calibration approach of multiple redox proxies, based on the enrichment sequence model of authigenic redox-sensitive element (RSE) governed by redox potential, has recently been proposed to calibrate redox thresholds in marine depositional systems. However, this assessment model often induces an overlapped threshold between anoxic–ferruginous and anoxic–euxinic conditions. Except for the redox potential, the enrichment of RSE is also controlled by its host phase. Thus, we introduced the enrichment degree and occurrence state model controlled by the host phase content into this approach to identify anoxic–euxinic conditions by an enrichment threshold of Mo (or U). Based on this method including double redox assessment models, we calibrated the thresholds of various redox conditions of the Chang 8–Chang 7 Members in the southern Ordos Basin. Subsequently, the effectiveness of previous bi-element proxies, the evolution of redox conditions, and their influencing factors were analyzed based on the calibrated thresholds. Results show that this method is applicable in the lacustrine strata. The cross plot of DOP_T (degree of pyritization based on the total Fe and S content) (or S_{EF})–Mo_{EF} (or U_{EF}) (enrichment factor) is suggested for calibrating thresholds of different redox conditions. Previous bi-element proxies are not suggested to be used again. There is a positive redox evolution sequence from oxic–suboxic (suboxidized) to anoxic–euxinic conditions in Chang 8–Chang 7 Members. Hydrothermal activity and paleoproductivity play different roles in the formation of redox conditions.

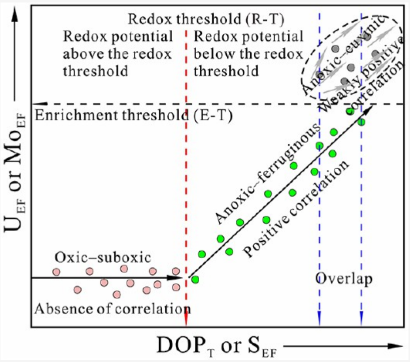

KEYWORDS: *Ordos Basin, Chang 7, internal calibration, redox thresholds, anoxic, euxinic*

1. INTRODUCTION

The chemical species characteristics of Fe (Fe_{py}/Fe_{HR} and Fe_{HR}/Fe_T),[1−3] degree of pyritization (DOP),[3,4] size of framboidal pyrite,[5,6] C_{org}/P ratio,[7,8] bimetallic element ratios (such as U/Th, V/Cr, and Ni/Co),[9] U and Mo isotopes,[10−12] and redox-sensitive element (RSE) enrichment factors have been frequently employed as redox proxies.[13−16] However, these redox parameters with various unified threshold values are not applicable to all strata and regions.[15,17] Algeo and Li (2020) suggested the internal cross-calibration approach of various redox proxies based on enrichment sequence models governed by the redox potential to calibrate the redox thresholds (T1, T2, and T3) (Figure 1a).[15] The T1, T2, and T3 values correlate to the commencement of authigenic Re, U, and Mo enrichments, respectively (Figure 1a). Compound covariation between the enrichment factors of RSEs and other redox proxies can be used to calibrate the onsets of the enrichment of RSEs as thresholds (Figure 1b).[15] Redox thresholds determined using this method in various strata match the unified redox potential in the redox ladder elucidated by Algeo and Li (2020).[15] This method has been suggested to apply to virtually all Phanerozoic marine depositional systems.[15]

Redox conditions of the bottom water were reclassified into five categories, namely, oxic, dysoxic (or hypoxic), suboxic (suboxidized), suboxic (subreduced), and euxinic conditions by Algeo and Li (2020).[15] Because the dysoxic conditions cannot be distinguished from oxic conditions by the element data[15] and the term "suboxic" is confusing,[19] we use the "oxic–suboxic (suboxidized)" to represent the redox conditions with the dissolved O_2 > 0 mL/L (Figure 1a). In addition, as both nonsulfidic (suboxic–subreduced) and sulfidic (euxinic) conditions are without dissolved O_2,[15] the anoxic–ferruginous

Received: August 27, 2022
Revised: November 19, 2022
Accepted: December 12, 2022
Published: December 30, 2022

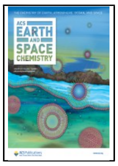

https://doi.org/10.1021/acsearthspacechem.2c00262

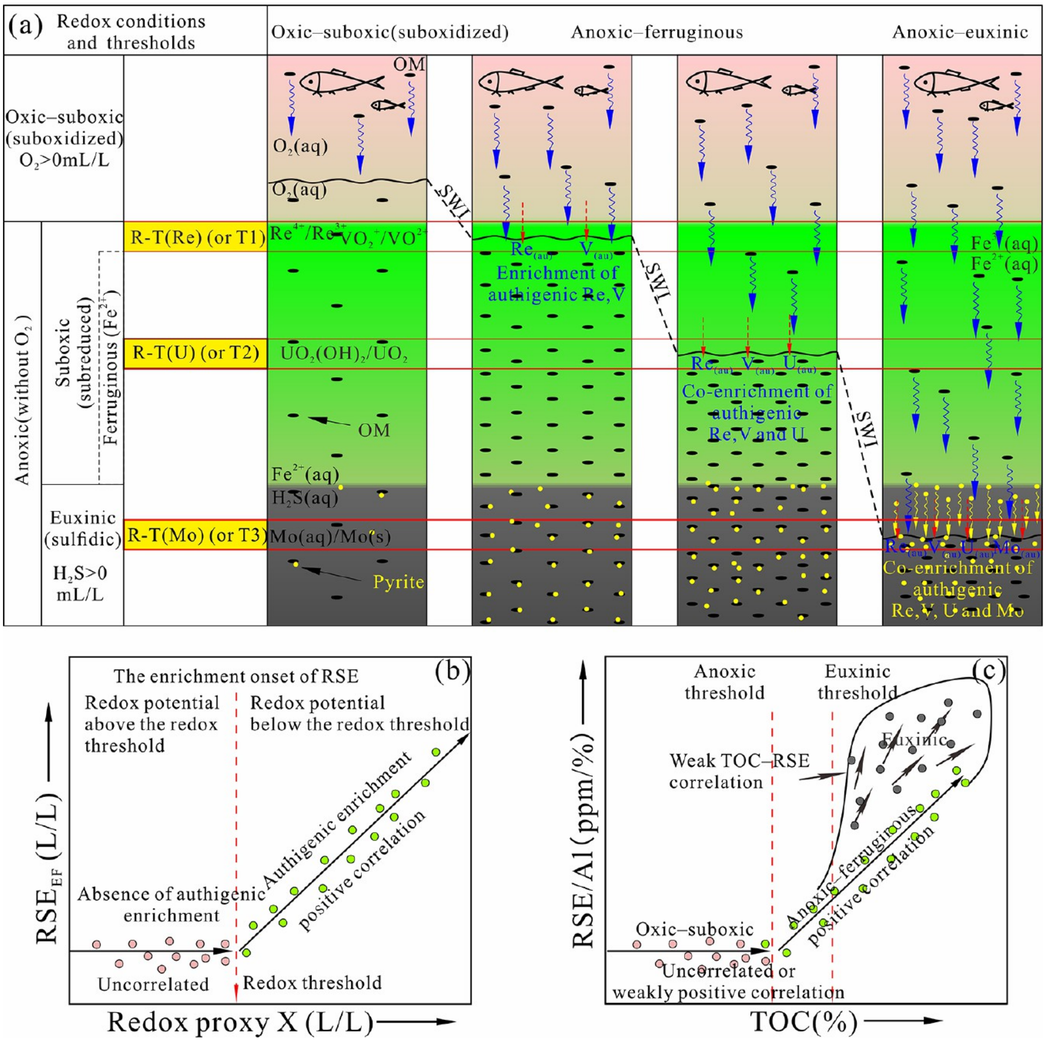

Figure 1. (a) Redox ladder scheme and (b, c) identification model of different redox conditions; the redox conditions and primary redox thresholds in (a) are reproduced from Algeo and Li (2020),[15] Copyright 2020 Elsevier; the identification patterns of redox conditions in (b) is reproduced from Algeo and Li (2020),[15] Copyright 2020 Elsevier; the identification patterns of redox conditions in (c) is reproduced from Algeo and Maynard (2004),[18] Copyright 2004 Elsevier; SWI: Sediment–water interface.

and anoxic–euxinic conditions are used to represent nonsulfidic and sulfidic anoxic conditions (Figure 1a), respectively.

The relative location fluctuation between the redox threshold and sediment–water interface (SWI) yields different co-enrichment combinations of RSEs under various redox conditions (Figure 1a). Additionally, compound covariation can identify RSE co-enrichment combinations (Figure 1b). However, the enrichment sequence model, which is only controlled by redox potential, is incapable of distinguishing between T2 and T3.[15] In addition, several redox proxies corresponding to redox thresholds calibrated solely by compound covariance in the correlation diagram do not have accurate values. Although this model has been recently utilized to calibrate the redox thresholds of a few lacustrine systems,[20] the abovementioned problems remain unresolved.

Except for the enrichment sequence of RSEs governed by the redox potential, their other geochemical characteristics, such as the enrichment degree and occurrence states controlled by organic matter, are distinct under various redox conditions.[18,21] RSEs (primarily V, U, and Mo) reside primarily in siliciclastic detrital fractions with low enrichment under oxic–suboxic (suboxidized) conditions, organic phases with moderate enrichment under anoxic–ferruginous (nonsulfidic) conditions, authigenic, RSE-bearing sulfide or oxyhydroxide phases with strong enrichment under anoxic–euxinic conditions (sulfidic).[18] Under different redox conditions, the varying enrichment degree and occurrence states of RSEs provide a range of covariation correlations between their concentration (RSE/Al) and total organic carbon (TOC) (Figure 1c).[18,21] Algeo and Maynard (2004) proposed the enrichment degree and occurrence state model (TOC–RSE relationships) of RSEs regulated by the organic host phase content (i.e., TOC) to assess redox conditions and calibrate the TOC thresholds of various redox circumstances (Figure 1c).[18] The TOC threshold was described as the TOC required to achieve redox thresholds adequate for trace metal buildup.[15,18] Overlap of the TOC ranges of adjacent redox patterns renders TOC unsuitable as a redox proxy for quantifying redox thresholds (Figure 1c). However, based on this model, anoxic–euxinic (or euxinic, sulfidic) conditions can be distinguished from anoxic–ferruginous (or suboxic–subreduced, nonsulfidic) conditions by different redox patterns (Figure 1c).

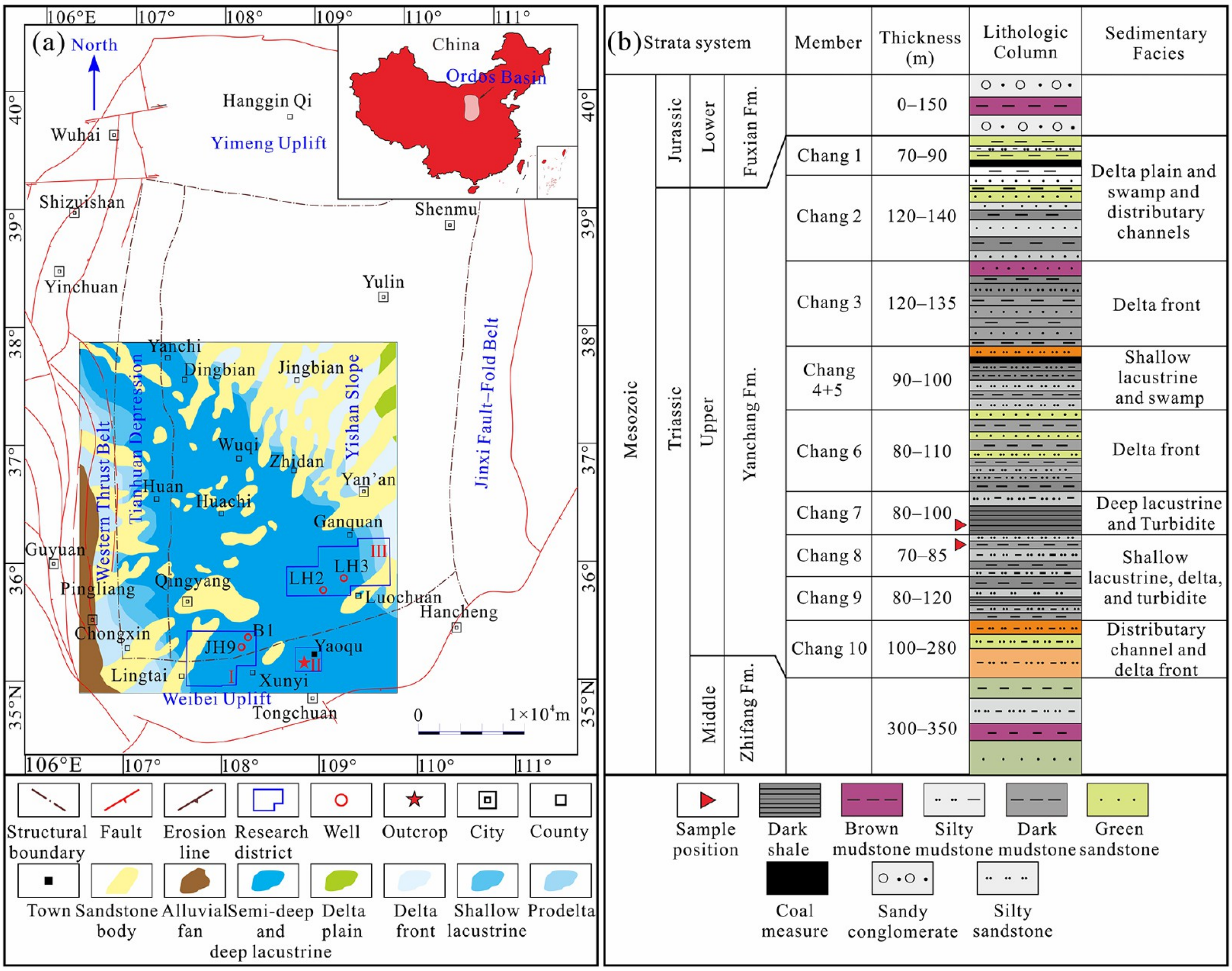

Figure 2. (a) Tectonic units, sedimentary facies of the Chang 7^3 sub-Member, research districts (I: Jinghe district, II: Tongchuan district, and III: Luohe district), and sampling positions. (b) Stratigraphic and lithological comprehensive column of the Yanchang Formation in the Ordos Basin. The sedimentary facies of Chang 7^3 sub-Member in (a) is reproduced from Yuan et al.(2015),[45] Copyright 2015 Creative Commons license CC BY-NC-ND 4.0. The distribution of tectonic units and faults is reproduced from Yang et al. (2012),[46] Copyright 2012 Creative Commons license CC BY-NC-ND 4.0 The stratigraphic and lithological comprehensive column graph was modified after Tang et al. (2014),[47] Copyright 2014 Elsevier. The sedimentary facies of different Members in panel (b) are after Tang et al. (2014)[47] and Zhang et al. (2021),[22] and it pertains only to data, not the figure itself.

The Upper Triassic Chang 8–Chang 7 Members in the Ordos Basin documented the entire sedimentary history from shallow to deep water in the paleolake.[22] The organic-rich shale and mudstone were deposited during the deposition of the Chang 7 Member. As these organic-rich fine-grained sedimentary rocks in the Chang 7 Member are primary Mesozoic source rocks,[23] target formation of shale oil exploration,[24] and records of biotic recovery of the freshwater ecosystem following the Permian–Triassic mass extinction in the Ordos Basin,[25] its redox conditions have been the focus of various studies.[25−31] However, the redox conditions in the Chang 7 Member as determined by the aforementioned redox proxies with defined threshold values were inconsistent, even at the same depth interval in the same well or geographically close to one another.[25−31] Therefore, Chang 8–Chang 7 Members were chosen to investigate the applicability of this method for calibrating thresholds of various redox states in lacustrine strata.

Given the issues created by both the above redox assessment models utilized for redox evaluation, we selected redox assessment models based on the behavioral difference of RSEs between adjacent redox conditions to calibrate the thresholds of various redox conditions in Chang 8–Chang 7 Members. Accordingly, the authigenic enrichment sequence model of RSEs was used to calibrate the redox thresholds R-T(Re) (or T1) and R-T(U) (or T2), and the enrichment degree and occurrence state model controlled by TOC were utilized to differentiate between anoxic–euxinic and anoxic–ferruginous conditions. Due to the redox couplings of other RSEs, the redox threshold is denoted as R-T(X) as opposed to the serial number proposed by Algeo and Li (2020),[15] where X represents the element. The redox proxies were utilized to calibrate the threshold values of redox conditions, such as the enrichment factors of RSEs (S, Re, V, U, and Mo), DOP_T, TOC, and pyrite content. As pyrite is also a host phase in which Mo and U reside in adsorbed or solid solution states,[18,32−36] it was considered as a proxy for calibrating the enrichment degree thresholds of RSEs under different redox conditions. Unlike Re, V, and U, the enrichment of Mo requires a H_2S-containing environment,[33,37−39] and its accumulation rate is related to the H_2S concentration.[40] Given this, our work primarily utilized Mo/Al–TOC and Mo/

Al−pyrite content correlation patterns to discriminate between anoxic−euxinic and anoxic−ferruginous conditions. The geochemical profile of redox proxies, mineral analysis, and paleontological observation was utilized to validate the reasonableness of the thresholds calibrated by the internal cross-calibration approach of numerous redox proxies. Based on these calibrated thresholds, the effectiveness of previous redox proxies such as V/Cr, V/(V + Ni), U/Th, Fe/Al, and C_{org}/P was also examined. In addition, the evolution of redox conditions in the Chang 8−Chang 7 Members and their influencing factors, such as hydrothermal activity and paleoproductivity, were also analyzed.

Our research is likely to contribute to the application of internal cross-calibration of multiple redox proxies to calibrate thresholds quantitatively between different redox conditions in the lacustrine strata and avoid ambiguous thresholds of redox conditions caused by the application of a single assessment model in this method.

2. GEOLOGICAL SETTING

The Ordos Basin is located to the west of the North China Craton (Figure 2a)[41,42] and spans 37 × 10^4 km^2 in area.[43] Based on the property of the basement and distribution of structural patterns, the Ordos Basin is divided into six second-order tectonic units:[44] the Yimeng Uplift in the north, Weibei Uplift in the south, Tianhuan Depression and Western Thrust Belt in the west, Jinxi Fault−Fold Belt in the east, and central Yishan Slope (Figure 2a).[44]

In the Late Triassic, the Ordos Basin changed from a craton basin with compressive margins to an intraplate remnant cratonic basin influenced by the Indo-Sinian tectonic movement in the Late Triassic.[23,48,49] Correspondingly, sedimentary facies in the basin changed from marine facies to terrestrial facies[48,50] and coincided with the deposition of the terrestrial strata of the Yanchang Formation with a thickness of 1−1.3 km.[48] The principal sedimentary facies of the Yanchang Formation are fluvial, deltaic, and lacustrine (Figure 2a,b). Based on their marker beds, sedimentary cycles, and lithological associations, the Yanchang Formation is divided into 10 Members from top to bottom (Figure 2b).[51] The Chang 7 Member is subdivided into three sub-Members, from bottom to top: the Chang 7^3, Chang 7^2, and Chang 7^1 sub-Members (Figure 2b).[45] Extensive dark-gray mudstones and black shale of the semi-deep and deep lacustrine facies in the Chang 7^3 sub-Member were deposited in the center and southern portions of the basin (Figure 2a).[45] These are the principal Mesozoic source rocks in the Ordos Basin.[23] Following the deposition of the Chang 7^3 sub-Member, the paleolake area began to decrease.[45] During the sedimentary epoch of the Chang 7^3 sub-Member, volcano and hydrothermal activity were also extremely active.[52,53]

Our research region includes the Jinghe, Tongchuan, and Luohe districts in the southern Ordos Basin. Jinghe district is situated at the southwestern confluence of the Yishan Slope and Weibei Uplift (Figure 2a). Tongchuan district is situated on the Weibei Uplift, whereas Luohe is situated southeast of the Yishan Slope belt (Figure 2a). In the Jinghe and Tongchuan districts, the lithofacies association of the Chang 8−Chang 7 Members is comparable based on well and outcrop lithology observations. Thin organic-rich mudstone layers and thick black shale series with numerous tuff interlayers develop in the Chang 7^3 sub-Member of the Jinghe and Tongchuan districts. In the Chang 7^1 and Chang 7^2 sub-Members of the Jinghe and Tongchuan districts, several thin layers a of gray mudstone and organic-rich black shale are also present.[22,54] In the Chang 7^3 sub-Member of the Luohe district, however, black mudstone is deposited, as opposed to shale. These mudstones are deposited beneath the semi-deep lacustrine environment that is next to the delta.[45] In addition, the Chang 7^1 and Chang 7^2 sub-Members of the Luohe district include both black and gray mudstone. Tuff beds are uncommon in the Chang 7 Member, Luohe district. The Chang 8−Chang 7 Members in the southern Ordos Basin document the progression from delta facies to deep-lacustrine facies.[22] To calibrate the thresholds of redox conditions in both strata, fine-grained sedimentary rocks from the Chang 8−Chang 7 Members of these districts were selected.

3. SAMPLES AND METHODS

3.1. Samples. Because the thresholds of various redox conditions are calibrated by the compound covariation patterns between RSEs enrichment factors and redox proxies, the samples used to calibrate the thresholds should represent a range of redox conditions. Therefore, 37 fine-grained sedimentary rocks of the Chang 8−Chang 7 Members in Jinghe district, Luohe district, and Tongchuan field profile in the southern Ordos Basin were systematically collected to calibrate the thresholds of different redox conditions based on the changes of lithofacies and sedimentary facies along the vertical dimension. Shale, mudstone, carbonaceous mudstone, argillaceous siltstone, and silty mudstone comprise these samples, which primarily represent shallow lacustrine facies to deep lacustrine facies. Two carbonatite samples from the Chang 7^3 sub-Member of the Motiangou outcrop in the Tongchuan district were also collected to eliminate the possible influence of hydrothermal activity on the ferrous mineral composition of the adjacent layer. The downhole core and outcrop samples were divided horizontally into multiple pieces for various observations, analyses, and tests. The majority of these fragment samples retain their original thickness, allowing interior laminae to be compared across various fragments. The thin intercalation and nodules are absent from the samples analyzed herein, and all downhole samples are cores.

3.2. Analytical Methods. A LECO CS-230 C and S analyzer were used to determine the organic matter and S content of fine-grained sedimentary rocks by analyzing the TOC and total S content (TS). The pretreatment of samples, experimental procedures, and quality standards for the TOC and TS analysis were in accordance with the Chinese national standard GB/T 19145−2003. X-ray fluorescence using an AB104L Axios-mAX wavelength dispersive X-ray fluorescence spectrometer was used to determine the major elemental content of fine-grained sedimentary rocks and tuffs. The abundance of trace elements in these samples was determined using inductively coupled plasma mass spectrometry on a PerkinElmer NexION 300D spectrometer. Detailed requirements for sample pretreatment, measuring range, and detection limit of major and trace elements followed the Chinese national standards GB/T 14506.30−2010, GB/T 14506.14−2010, and GB/T 14506.28−2010, respectively.

At least 10 g of sample for the major and trace element analyses was ground into powder in an agate ball mill and then screened using a 200-mesh screen. Accordingly, 50 mg of each powder sample was weighed for 24 h of digestion in a Teflon bomb containing a mixture of 30% HF and 68% HNO_3 at 190

°C.[55] Excess solvent was then evaporated at 130 °C for 3 h, and the process was repeated again.[55] The sample was then redissolved with 2 mL of 6 mol/L HNO_3 in Teflon bombs with caps at 150 °C for 24 h.[55] Subsequently, the sample was quantitatively transferred into a 50 mL plastic bottle and diluted to 50 mL with deionized distilled water in preparation for the examination of trace elements. Because HNO_3 and HF are toxic and caustic, it is necessary to wear protective gear when using them and to avoid skin and eye contact. Accordingly, these substances should be evaporated in a fume cupboard.

Fine-grained sedimentary rocks and carbonatite were studied by X-ray diffraction (XRD) on a Bruker D8 Focus equipped with a ceramic X-ray tube containing Cu targets. The X-ray tube had a working voltage of 40 kV and working current of 40 mA. The XRD detection angle of the entire rock ranged from 4.5 to 50° (2θ) with a step of 0.02° (2θ), and the scanning speed was 2°/min (2θ). In addition, the XRD analysis complied with China Petroleum and Natural Gas Industry Standard SY/T5163−2018 for sample preparation, experimental operation standards, and raw data processing criteria.

Optical microscopy was used to observe the microscopic structure of carbonatite. C and O isotope analysis was carried out to detect the possible origin of carbonatite. In addition, a Leica 4500 MP polarizing microscope with an ultraviolet light source and photographic system was used to observe the microstructure of carbonatite under transmission light, using 2.5× objective lenses. Moreover, the $\delta^{13}C$ and $\delta^{18}O$ of carbonatite were examined using an Elementar Isoflow-Precision online preparation continuous flow-stable isotope mass spectrometer. Sample pretreatment and data quality adhered to the China Petroleum and Natural Gas Industry Standard SY/T5238−2008.

The TOC and TS tests, C and O isotope analysis, and optical microscopy observations were conducted at the Laboratory of Petroleum Resources and Prospecting, China University of Petroleum, Beijing. XRD of the entire rock was completed at the Microstructure Laboratory for Energy Materials of the China University of Petroleum, Beijing. In addition, major and trace element content was analyzed at the Analytical Laboratory of the Beijing Research Institute of Uranium Geology.

3.3. Calculation of Redox Proxies.

An Al-normalized enrichment factor was adopted to evaluate the enrichment degree of trace elements.[13−15,56] The corresponding formula is[14,15]

$$X_{EF} = \left(\frac{X}{Al}\right)_{sample} / \left(\frac{X}{Al}\right)_{reference\ material} \tag{1}$$

where X represents the abundance of trace elements. This formula was also used to compute the enrichment factors for Fe_2O_3 and S to determine their degree of enrichment. The elemental composition of clay and shale samples reported by Wedepohl (1971)[57] or upper continental crust (UCC)[58] is frequently employed as a reference material to normalize the abundance of redox-sensitive trace elements. As these reference materials lack definite redox conditions, 10 modern humin-rich sediment samples from the Black Sea reported by Lüschen (2004)[59] were used as reference materials to determine the degree of RSE enrichment relative to the reference material with definite redox conditions. These samples from Station-7 were deposited in a euxinic (sulfidic) environment at depths of 137.5, 138.25, 139.25, 140.25, 141.25, 141.75, 142.25, 142.75, 143.5, and 144.5 cm.[15] Accordingly, TOC, TS, Al_2O_3, Fe_2O_3, Re, V, U, and Mo have averages of 22.08%, 2.29%, 9.01%, 3.80%, 0.0597 ppm, 250 ppm, 15.7 ppm, and 101.0 ppm, respectively. In addition, the enrichment coefficient of RSEs normalized by the elemental composition of the upper continental crust (UCC) reported by Rudnick and Gao (2014)[58] is included in the Supporting Information to assist comparison across different studies (Table S1).

The following equation is based on the mineral content calculation approach published by van Kaam-Peters (1998):[60]

$$\text{pyrite (\%)} = [(100 - 1.5 \times \text{TOC}) \times \text{pyrite}_{XRD}]/100 \tag{2}$$

where pyrite_{XRD} indicates the relative proportion of minerals determined by XRD and 1.5 × TOC is the quantity of organic matter. The other mineral content is calculated in the same manner as pyrite. DOP_T is frequently used in place of DOP to evaluate the mineralization degree of pyrite in samples that have not been subjected to chromium reduction.[15,61] Its calculation equation is[15]

$$DOP_T = [(S/32.06)/2]/(Fe_T/55.845) \tag{3}$$

where S is the total sulfur, Fe_T is the total iron, 32.06 is the relative atomic mass of S, and 55.845 is the relative atomic mass of Fe.

4. RESULTS

4.1. TOC.

In the Jinghe and Tongchuan districts, Chang 8 Member sedimentary rocks contain mudstone, carbonaceous mudstone, silty mudstone, and argillaceous siltstone. The TOC of these fine-grained sedimentary rocks ranges from 0.25 to 3.26%, with an average of 1.20% (Table S2). The black mudstone was deposited at the base of the Chang 7^3 sub-Member in the Jinghe, Tongchuan, and Luohe districts as the paleolake began to expand. The TOC of this mudstone ranges from 0.76 to 6.40%, with an average of 3.19% (Table S2). After the deposition of the mudstone layer in the Chang 7^3 sub-Member, the organic-rich black shale was deposited in the Jinghe and Tongchuan districts as the paleolake spread and deep lake facies evolved. The TOC of this shale ranges from 9.16 to 33.84%, with an average of 22.58% (Table S2). Following the deposition of shale within the Chang 7^3 sub-Member, the paleolake began to shrink. During the shrinkage period of the paleolake, the Chang 7^1−Chang 7^2 sub-Members in parts of the Jinghe district continued to develop a thin shale layer. Accordingly, the average TOC values of the thin shale layer in the Chang 7^1 and Chang 7^2 sub-Members range from 14.03 to 26.36%, with an average of 20.03% (Table S2). Moreover, the TOC of mudstone from the Chang 7^2 sub-Member is 1.63% (Table S2).

4.2. Enrichment Degree of RSE.

RSEs such as Fe, S, Re, V, U, and Mo are typically employed to evaluate redox conditions.[13,14,18,21,37,39,62,63] In addition, the Fe_2O_{3EF} (total Fe), S_{EF}, Re_{EF}, V_{EF}, U_{EF}, and Mo_{EF} of the Chang 7 Member shale are generally much higher than those of other fine-grained sedimentary rocks, which corresponds to the distribution of the TOC value of fine-grained sedimentary rocks (Table S3). The Fe_2O_{3EF}, S_{EF}, Re_{EF}, V_{EF}, U_{EF}, and Mo_{EF} of the Chang 7 sub-Member shale are 1.515−9.197 (average: 4.210), 1.281−11.442 (average: 4.942), 0.060−0.550 (average: 0.325), 0.371−2.243 (average: 1.179), 0.556−13.830 (average:

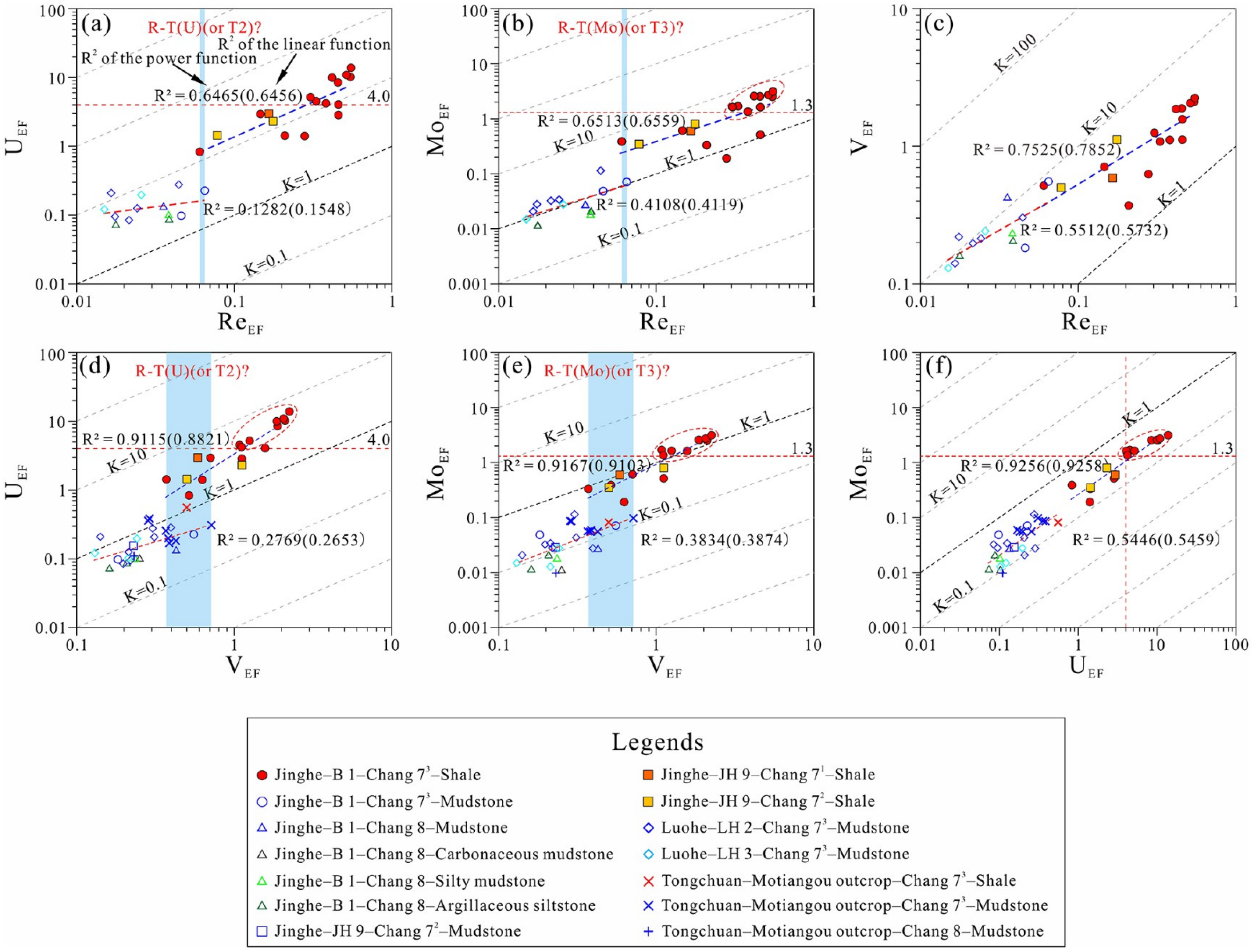

Figure 3. (a−f) Cross plots of Re_{EF}−V_{EF}−U_{EF}−Mo_{EF} of fine-grained rocks from the Chang 8−Chang 7 Members in the southern Ordos Basin.

4.893), and 0.082−3.124 (average: 1.314), respectively (Table S3).

4.3. Redox Proxy Value, Ferrous-Bearing, and S-Bearing Mineral Content of Fine-Grained Sedimentary Rocks of Chang 8−Chang 7 Members.

In accordance with the distribution characteristics of the TOC and RSEs of fine-grained sedimentary rocks in the Chang 8−Chang 7 Members, the pyrite content and its related redox proxies, such as DOP_T and Fe_{mol}/S_{mol}, of shale in the Chang 7 Member are considerably higher or lower than those of other fine-grained sedimentary rocks (Tables S2 and S3). The pyrite content, DOP_T, and Fe_{mol}/S_{mol} of shale in the Chang 7 sub-Member are 5.68−25.81 (average: 15.05), 0.568−1.048 (average: 0.860), and 0.48−0.88 (average: 0.60), respectively (Tables S2 and S3). The siderite content of the majority of fine-grained Chang 8−Chang 7 Members is <10% (Table S2). The gypsum content of fine-grained Chang 8−Chang 7 Member rocks is generally low, ranging from 0.00 to 2.98% (average: 0.10%) (Table S2). Other redox proxies such as V/Cr, V/(V + Ni), U/Th, Fe/Al, and C_{org}/P of shale from the Chang 7 Member are not considerably higher than those of other fine-grained sedimentary rocks from the Chang 8−Chang 7 Members (Table S3). Accordingly, the V/Cr, V/(V + Ni), U/Th, Fe/Al, and C_{org}/P ratios of shale in the Chang 7 sub-Member are 1.83−8.46 (average: 5.39), 0.76−0.91 (average: 0.87), 1.13−20.87 (average: 8.10), 0.24−5.13 (average: 1.37), and 112.08−884.99 (average: 360.21), respectively (Table S3).

4.4. Hydrothermal and Paleoproductivity Proxy Values of Fine-Grained Sedimentary Rocks of Chang 8−Chang 7 Members.

Al/(Al + Fe + Mn), (Fe + Mn)/Ti, Fe_2O_3/TiO_2, and MnO/TiO_2 are frequently utilized to monitor hydrothermal activity.[52,64−66] Accordingly, the Al/(Al + Fe + Mn), (Fe + Mn)/Ti, Fe_2O_3/TiO_2, and Mn/TiO_2 ratios of fine-grained rocks in Chang 7−Chang 8 Members are 0.16−0.80 (average: 0.51), 5.38−107.91 (average: 30.18), 4.58−92.07 (average: 25.45), and 0.03−2.71 (average: 0.37), respectively (Table S4).

Cu, Ni, and P are associated with organic C sinking flow and paleoproductivity in fine-grained rocks.[21,67] Their proxies, including Cu/Ti (or Cu/Al), Ni/Ti (or Al), (Cu + Ni)/Ti (or Al), and P/Ti (or Al), were frequently used to estimate paleoproductivity.[68−71] Therefore, Cu/Ti, Ni/Ti, and P/Ti are adopted to track the evolution of paleoproductivity in Chang 7−Chang 8 Members. Accordingly, the Cu/Ti, Ni/Ti, and P/Ti ratios of fine-grained rocks in the Chang 7−Chang 8 Members are 0.64×10^{-2}−16.41×10^{-2} (average: 3.93×10^{-2}), 0.49×10^{-2}−3.27×10^{-2} (average: 1.42×10^{-2}), and 0.04−2.12 (average: 0.58), respectively (Table S4).

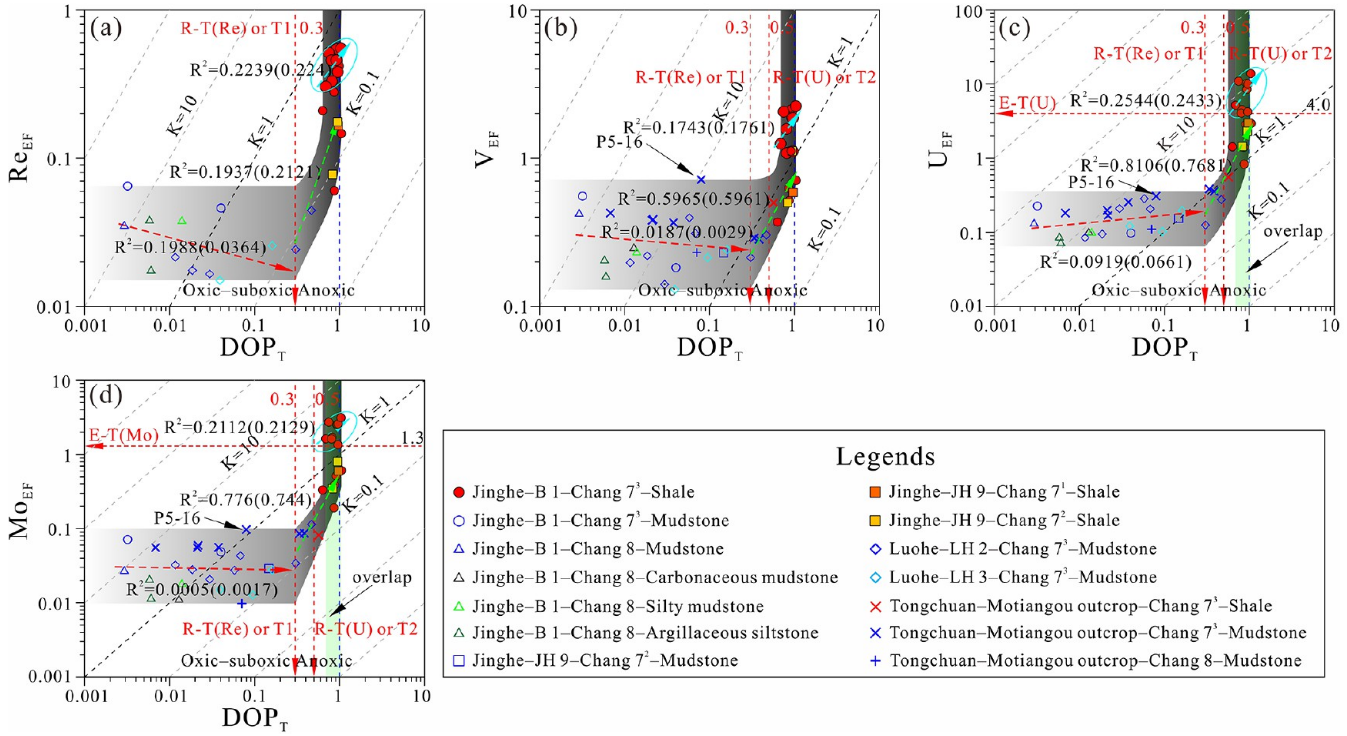

Figure 4. (a–d) Cross plots of DOP_T–Re_{EF}–V_{EF}–U_{EF}–Mo_{EF} of the Chang 8–Chang 7 fine-grained sedimentary rocks in the southern Ordos Basin. The larger red solid cycles in (a) and (b) are the shale with $Mo_{EF} > 1.3$ and $U_{EF} > 4.0$.

5. DISCUSSION

5.1. Calibration of Thresholds for Different Redox Conditions.

5.1.1. Redox Thresholds between Oxic–Suboxic (Suboxidized) and Anoxic–Ferruginous Conditions. Due to the different relative position relationships between the redox threshold and SWI, which result in different co-enrichment combinations of RSEs in surficial sediments under different redox conditions (Figure 1a), the covariation relationships among RSEs can be used to identify the redox conditions of bottom water. Because the Re abundance of some fine-grained sedimentary rocks is below the detection limit of our instruments (<0.002 ppm), their redox states cannot be established by the correlations of Re_{EF}–U_{EF}–Mo_{EF} (Figure 3a,b). The redox enrichment potential of V is slightly less than that of Re within the redox potential range of threshold T1, as determined by Algeo and Li (2020),[15] and the positive correlation between R_{EF} and V_{EF} demonstrates that V can be utilized to calibrate the threshold of anoxic–ferruginous conditions (Figure 3c).

The correlation of U_{EF}–Re_{EF} and U_{EF}–V_{EF} shows that the U_{EF} of shale with a reasonably high U_{EF} ($U_{EF} \geq 0.556$) is positively correlated with Re_{EF} and V_{EF} within the ranges of $Re_{EF} \geq 0.060$ and $V_{EF} \geq 0.371$, respectively (Figure 3a,d). This suggests that these shales were deposited at depths where the redox potential was less than R-T(U) (T2). The U_{EF} of other fine-grained rocks with relatively low U_{EF} (≤ 0.074) demonstrates an uncorrelated distribution with an increase in Re_{EF} and V_{EF} within $Re_{EF} \leq 0.065$ and $V_{EF} \leq 0.717$, showing that these fine-grained rocks were deposited in waters with a redox potential greater than R-T(U) (T2) (Figure 3a,d). Except for the Chang 7^3 sub-Member in the Tongchuan district, the Mo_{EF} of other shales with reasonably high Mo_{EF} ($Mo_{EF} \geq 0.191$) is positively correlated with their Re_{EF} and V_{EF} within the ranges of $Re_{EF} \geq 0.060$ and $V_{EF} \geq 0.371$, respectively (Figure 3b,e). The Mo_{EF} of shale in the Chang 7^3 sub-Member of the Tongchuan district and other fine-grained rocks with relatively low Mo_{EF} is uncorrelated with their Re_{EF} and V_{EF} between $Re_{EF} \leq 0.065$ and $V_{EF} \leq 0.717$ (Figure 3b,e). Due to the strong association between Mo_{EF} and U_{EF} (Figure 3f), anoxic–ferruginous and anoxic–euxinic conditions cannot be separated by the covariation of Re_{EF}–V_{EF}–U_{EF}–Mo_{EF} (Figure 3a,b,d,e).

The U_{EF} of the majority of shale in the threshold range is >1.0 (Figure 3a,d and Table S3), indicating that the overlap between probable R-T(U) (T2) and R-T(Mo) (T3) may not come from restricted U^{6+} concentration and rapid transition, as suggested by Algeo and Li (2020).[15] Although it was also believed that the reduction of U(VI) was related to the reduction of Fe(III) mediated by microorganisms,[72] the positive relationship between U_{EF} and Mo_{EF} under various redox conditions may be related to the sulfate reduction of organic matter and formation of pyrite. $U_2(CO_3)_3^{4-}$ can be converted to UO_2 by H_2S from sulfate reduction in sediments,[73] which is also required for the formation of particle-reactive thiomolybdates,[33] which may result in a positive relationship between the U_{EF} and Mo_{EF} of these organic-rich shales.

The enrichment of authigenic Re in sediments under anoxic conditions appears to be regulated only by redox conditions,[74] in contrast to the enrichment of V, U, and Mo, which is controlled by numerous enrichment mechanisms under various anoxic conditions.[13,18,21,75] In addition, the abundance of Re in the modern euxinic Black Sea sediment (0.0597 ppm) is substantially higher than that of the upper continental crust (0.198 ppt).[58] These disparities may result in a $Re_{EF} < 1$ for all samples, although the corresponding V_{EF}, Mo_{EF}, and U_{EF} values vary widely between 0.01 and 14. It is observed that the $Re_{EF\text{-}UCC}$ (normalized by the upper continental crust) of all

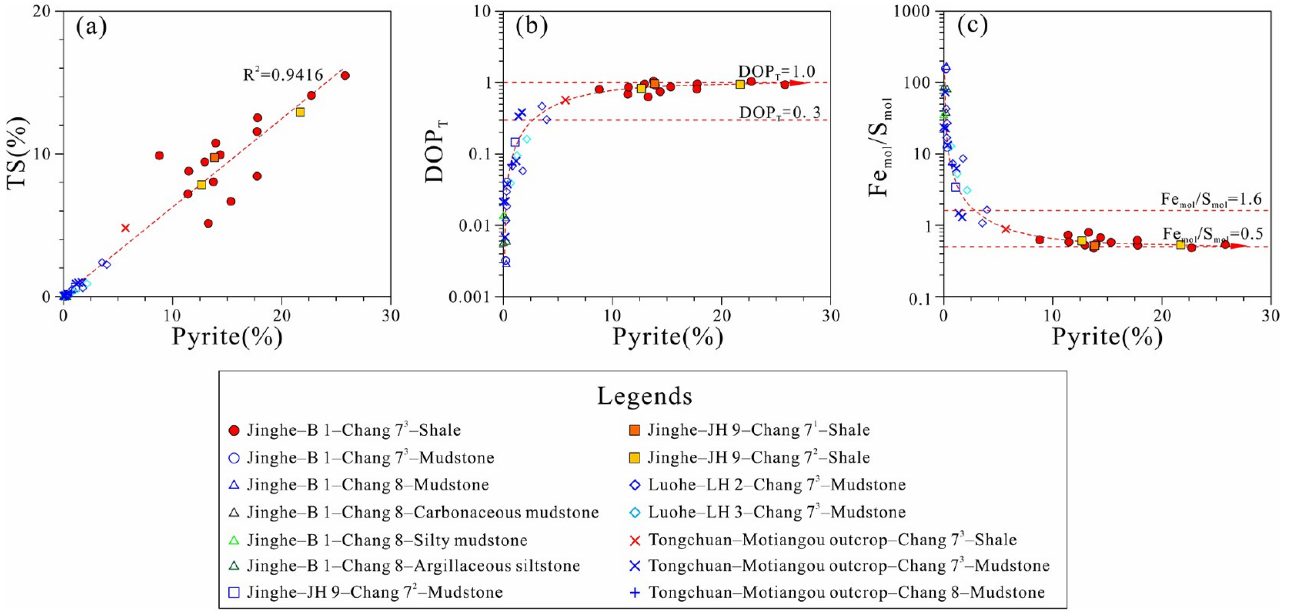

Figure 5. (a−c) Cross plots of the pyrite content−TS−DOP$_T$−Fe$_{mol}$/S$_{mol}$ of fine-grained sedimentary rocks from the Chang 8−Chang 7 Members in the southern Ordos Basin.

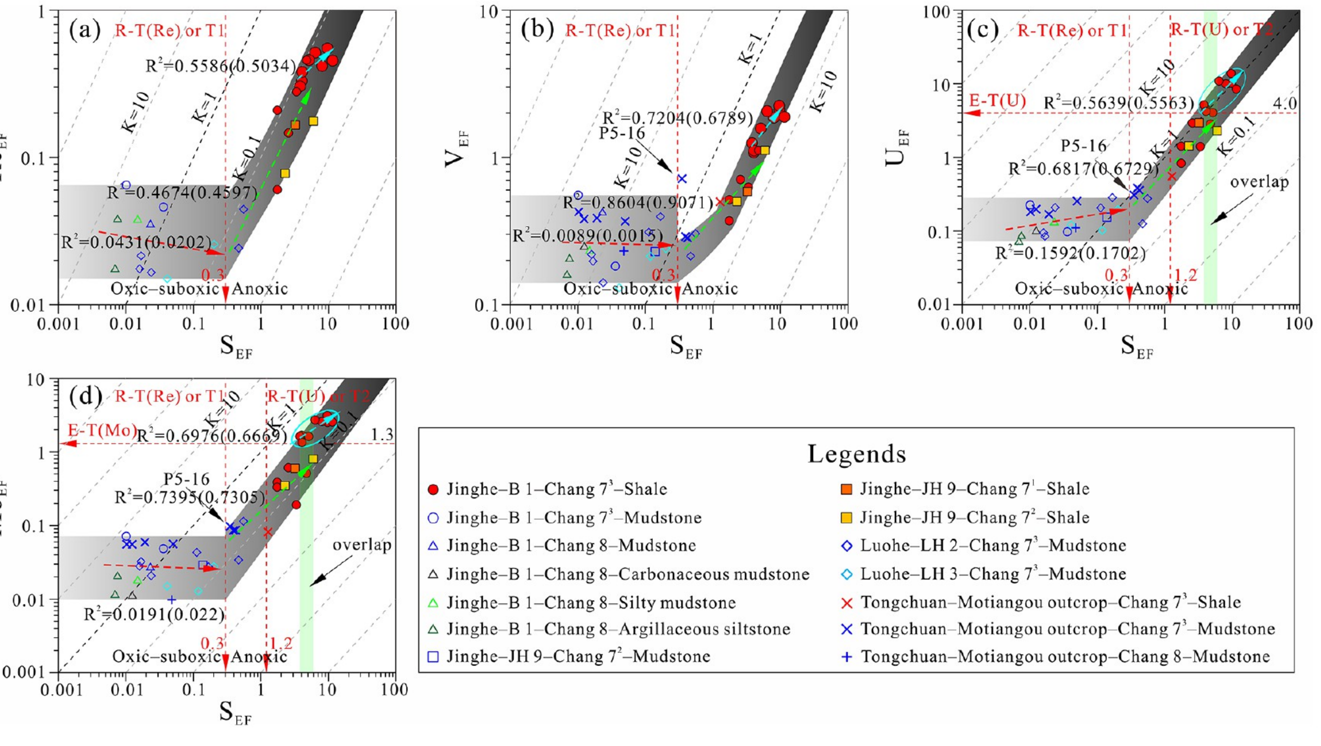

Figure 6. (a−d) Cross plots of S$_{EF}$−Re$_{EF}$−V$_{EF}$−U$_{EF}$−Mo$_{EF}$ of the Chang 8−Chang 7 fine-grained sedimentary rocks in the southern Ordos Basin. The larger red solid cycles in (a) and (b) are the shale with Mo$_{EF}$ > 1.3 and U$_{EF}$ > 4.0.

samples with Re abundance above the detection limit is >1 (Table S1), whether they are organic-rich shales or argillaceous siltstones (Table S1). This indicates that redox conditions cannot be evaluated solely based on the enrichment degree of RSEs without the covariation patterns that reflect the redox conditions between them.

DOP$_T$ can also be used as a redox scale to calibrate thresholds in place of DOP, except for that the co-enrichment combination of Re, V, U, and Mo is utilized to calibrate the redox thresholds.[15,17] Re$_{EF}$, V$_{EF}$, U$_{EF}$, and Mo$_{EF}$ of fine-grained rocks have an uncorrelated distribution within a relatively low value range as DOP$_T$ increases within DOP$_T$ < 0.3 (Figure 4a−d). Their relatively low values of Re$_{EF}$, V$_{EF}$, U$_{EF}$, and Mo$_{EF}$ indicate that they may deposit under oxic−suboxic (sub-oxidized) conditions, particularly when they have a relatively low V$_{EF}$.[16] However, they increase with DOP$_T$ > 0.3 (Figure 4a−d), showing that the authigenic enrichment of Re, V, U, and Mo begins at DOP$_T$ = 0.3. The U$_{EF}$ and Mo$_{EF}$ of fine-

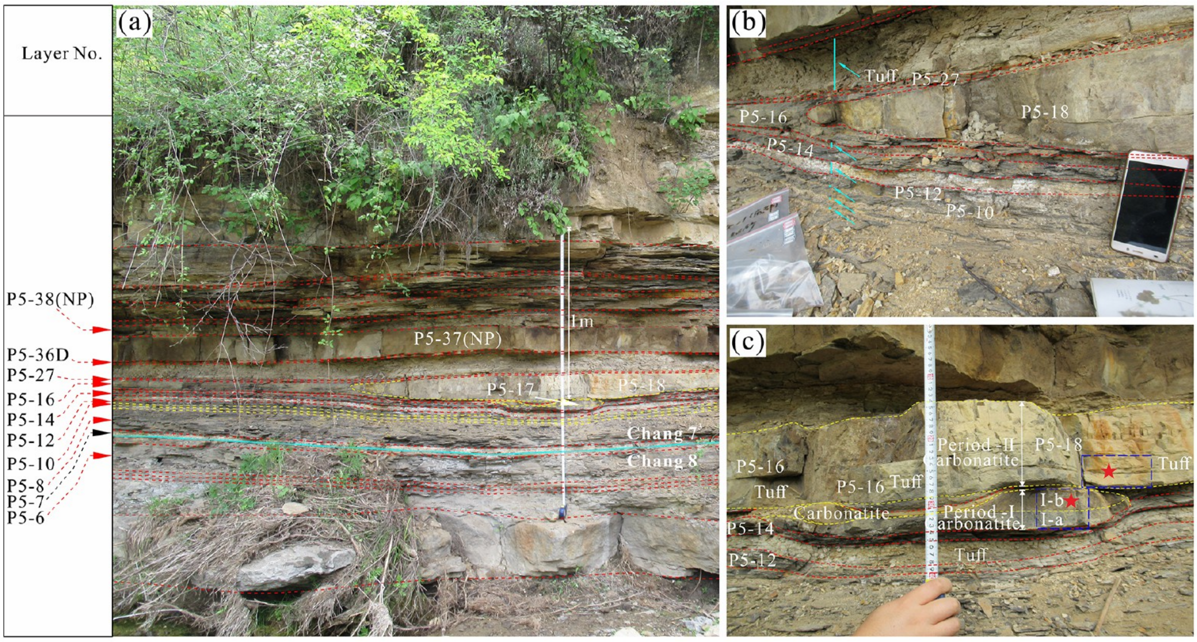

Figure 7. Photographs of the Motiangou outcrop of Chang 8−Chang 7 Members in Tongchuan district. (a) Layer no. in the outcrop; (b), (c) contact relationships among the carbonatite and the adjacent layers; the blue dashed line boxes in (c) are the sampling positions; red stars in (c) are the position where the XRD analysis is conducted; the I-a and I-b in (c) are the argillaceous carbonatite and clay-bearing carbonatite, respectively.

grained rocks with a DOP_T between 0.3 and 0.5 demonstrate a distinct distribution with increasing Re_{EF} and V_{EF}, i.e., U and Mo are not co-enriched with Re and V. (Figure 3a,b,d,e). In accordance with the enrichment sequence and co-enrichment combination (Figure 1a), DOP_T corresponds to the R-T(Re) (T1) of fine-grained rocks in the Chang 7 Member at 0.3 (Figure 4a−d). The U_{EF} of fine-grained rocks of the Chang 7 Member within $DOP_T > 0.5$ is positively correlated with Re_{EF} and V_{EF} variation and is considerably greater than that of fine-grained Chang 7 Member rocks with $DOP_T < 0.5$ (Figure 3a,d). However, the Mo of shale initially deposited in the Chang 7^3 sub-Member of the Tongchuan district within $DOP_T > 0.5$ is not co-enriched with V (Figures 3e and 4d). This indicates that the redox potential of bottom water is below R-T(U) (T2) when the DOP_T of these fine-grained sedimentary rocks is >0.5. Accordingly, DOP_T corresponds to R-T(U) (T2) at 0.5 in the Chang 8−Chang 7 Members, based on the co-enrichment of Re, V, and U (Figure 3a,d). As a result of the positive correlation between the U_{EF} and Mo_{EF} of all fine-grained sedimentary rocks (Figure 3f), the DOP_T corresponding to R-T(Mo) (T3) cannot be calibrated by their enrichment sequence and co-enrichment combination (Figure 4c,d).

Except for pyrite, only four samples contain other S-containing minerals, such as gypsum, with a maximum content of 2.98% (Table S2). The majority of these rocks contain <1% gypsum (Table S2). Moreover, TS, DOP_T, and Fe_{mol}/S_{mol} are favorably linked with the pyrite content (Figure 5a−c), suggesting that S exists primarily as a crucial electron carrier in the low valence in pyrite (FeS_2). Herein, S_{EF} has also been employed as a redox proxy to calibrate redox thresholds. The Re_{EF}, V_{EF}, U_{EF}, and Mo_{EF} of fine-grained sedimentary rocks have an uncorrelated distribution with increasing S_{EF} within $S_{EF} < 0.3$ (Figure 6a−d). However, they present a positive correlation with S_{EF} within $S_{EF} > 0.3$ (Figure 6a−d). This indicates that Re, V, U, and Mo are co-enriched with S if the S_{EF} of these fine-grained sedimentary rocks is >0.3. Accordingly, S_{EF} corresponds to R-T(Re) at a value of 0.3. Calibration of the S_{EF} corresponding to R-T(U) is identical to that of DOP_T. The S_{EF} equivalent to R-T(U) is 1.2 based on the co-enrichment difference between U and Mo as the V_{EF} and Re_{EF} increase (Figure 3a,b,d,e). In addition, the S_{EF} corresponding to R-T(Mo) (T3) cannot be confirmed by the enrichment sequence of the relationships of U_{EF}−S_{EF} and Mo_{EF}−S_{EF} due to the co-enrichment between U and Mo of most shales (Figure 3f).

The enrichment onset of Re, V, U, and Mo corresponding to the same DOP_T and S_{EF} may be related to the deposition, reduction, and combination with S of the reactive Fe in pyrite. Under anoxic−ferruginous bottom water conditions, the authigenic Re co-enriches with the reactive Fe of pyrite. Subsequently, the authigenic V, U, and Mo are sequentially deposited with the reduction and combination with S of the reactive Fe of pyrite. Therefore, the redox threshold calibrated by the relationship between DOP_T (or S_{EF}) and RSE enrichment factors represents the beginning of anoxic−ferruginous conditions. It also suggests that S_{EF} can indicate the redox conditions of bottom water when it is predominantly coupled with the reactive Fe of pyrite.

The DOP_T of the mudstone layer no. P5-16 (in which sample no. P5-16 is situated) of the Chang 7^3 sub-Member in the Tongchuan outcrop is <0.30 (Figure 4), although its S_{EF} is >0.3 (Figure 6), indicating incompatible redox conditions at the same depth. However, mineral analysis, paleontological observation, and variation of redox proxies in the field profile indicate that mudstone layer no. P5-16 was deposited under anoxic−ferruginous conditions, and its lower DOP_T was induced by the formation of hydrothermal siderite ($FeCO_3$).

The siderite content of layer no. P5-16 is as high as 12.52%, which is considerably higher than the siderite content of other layers in the outcrop, which ranges from 0 to 6.46%, whereas the pyrite (FeS_2) content of layer no. P5-16 is 1.16%. The comparatively high siderite content in layer no. P5-16 may be

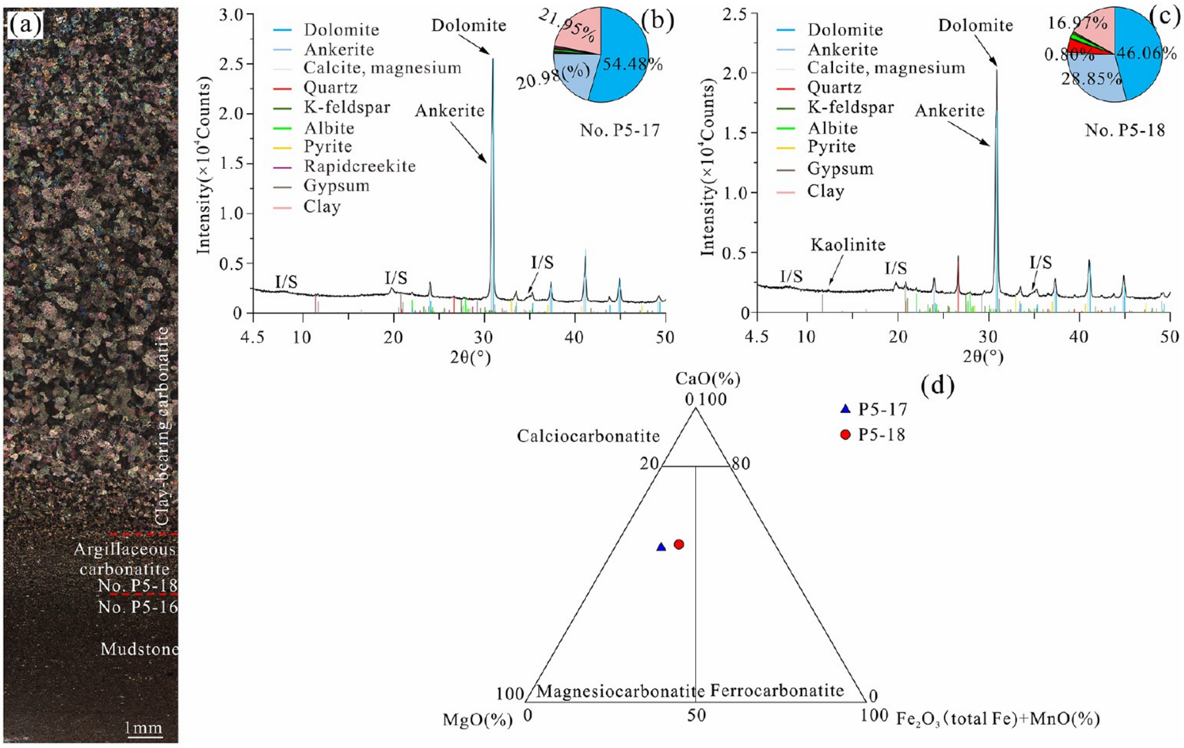

Figure 8. (a) Orthogonally polarized micrograph no. P5-18; (b), (c) XRD diffraction patterns; (d) classification of carbonatite rocks based on the composition of CaO−MgO−Fe_2O_3 (total Fe) + MnO in the Chang 7^3 sub-Member in the Motiangou outcrop of the Tongchuan district. The classification criteria of CaO−MgO−Fe_2O_3 (total Fe) + MnO is after Le Maitre et al. (2002),[78] and it pertains only to data, not the figure itself.

the product of hydrothermal fluid from the eruption of two-period igneous carbonatite (layer no. P5-17 corresponding to Period-I and layer no. P5-18 corresponding to Period-II) (Figure 7a−c). The two-period carbonatite layers and underlying mudstone layers exhibit a structure similar to that of channels with erosion structures, with the lithological association consisting of mudstone, argillaceous carbonatite, and clay-bearing carbonatite in the cross section from bottom to top (Figures 7c and 8a). Fine-grained carbonates (grain size < 1 mm), which predominantly comprise dolomite and ankerite (total content > 70%) (Figure 8b,c), exhibit an allotriomorphic granular texture (Figure 8a) distinct from the radiate and spherical texture in the oval carbonate concretions of the Chang 7 Member.[76,77]

These carbonatites are magnesiocarbonatites based on their CaO, MgO, Fe_2O_3, and MnO composition (Figure 8d).[78] The $\delta^{13}C_{V\text{-}PDB}$ and $\delta^{18}O_{V\text{-}PDB}$ of the carbonatite are 2.1‰ and −13.9‰, respectively, which are comparable to those of the hydrothermal calcite in St. Vincent, Peru.[79] According to the thickness, the eruption of Period-II carbonatite was more intense than the Period-I eruption (Figure 7a,c). The intense eruption eroded a portion of the underlying mudstone layer no. P5-16 (Figure 7b,c) and wedged the carbonatite into mudstone layer no. P5-16 at the lateral contact area (Figure 7a,b). Before the relatively intense eruption of Period-II carbonatite (no. P5-18) or after the relatively weak eruption of Period-I carbonatite (no. P5-17), considerable amounts of CO_2-rich hydrothermal fluids may have been released from hydrothermal vents into the bottom water, resulting in the deposition of hydrothermal siderite.

The variation of Al/(Al + Fe + Mn), (Fe + Mn)/Ti, MnO/TiO_2, and Fe_2O_3/TiO_2 curves indicates that hydrothermal activity occurred after the first mudstone layer no. P5-8 in the Chang 7^3 sub-Member and increased considerably after the eruption of carbonatite (Figure 9). For classic hydrothermal sediments, Al/(Al + Fe + Mn) is typically low (generally <0.4) and (Fe + Mn)/Ti is typically high (generally >15),[52,65] as are MnO/TiO_2 and Fe_2O_3/TiO_2.[65] Al/(Al + Fe + Mn) decreases from 0.78 to 0.80 in the no. P2-5-18 and P5-8 mudstone layers to 0.35 in mudstone layer no. P5-16 (Figure 9). Correspondingly, their (Fe + Mn)/Ti ratio increases from 5.38−6.95 to 46.25 (Figure 9). Changes in MnO/TiO_2 and Fe_2O_3/TiO_2 follow the same pattern as (Fe + Mn)/Ti (Figure 9). This suggests that the hydrothermal fluid began occurring in the bottom water following the no. P5-8 mudstone layer and became the predominant fluid in the no. P5-16 mudstone layer. As the hydrothermal fluid contains high concentrations of reducing substances, such as Fe^{2+} and Mn^{2+},[80,81] it can directly convert the oxic−suboxic (suboxidized) conditions into anoxic−ferruginous conditions. Consequently, the no. P5-16 mudstone layer was deposited under anoxic−ferruginous conditions.

The presence of benthic ostracod fossils in mudstone layers no. P5-12 and P5-14 but not in mudstone layer no. P5-16 shows that the redox conditions of the bottom water altered dramatically when the mudstone layer no. P5-16 with $S_{EF} > 0.3$ was deposited (Figures 9 and 10). During the deposition of mudstone layers no. P5-14 and P5-12, the redox conditions of the bottom water fluctuated between oxic−suboxic (suboxidized) and anoxic−ferruginous conditions. This may be triggered by the reducing fluid generated by the initial hydrothermal activity. The alternating fluctuation of redox conditions may have resulted in the ongoing demise of some ostracods as the bottom water had little to no dissolved O_2.

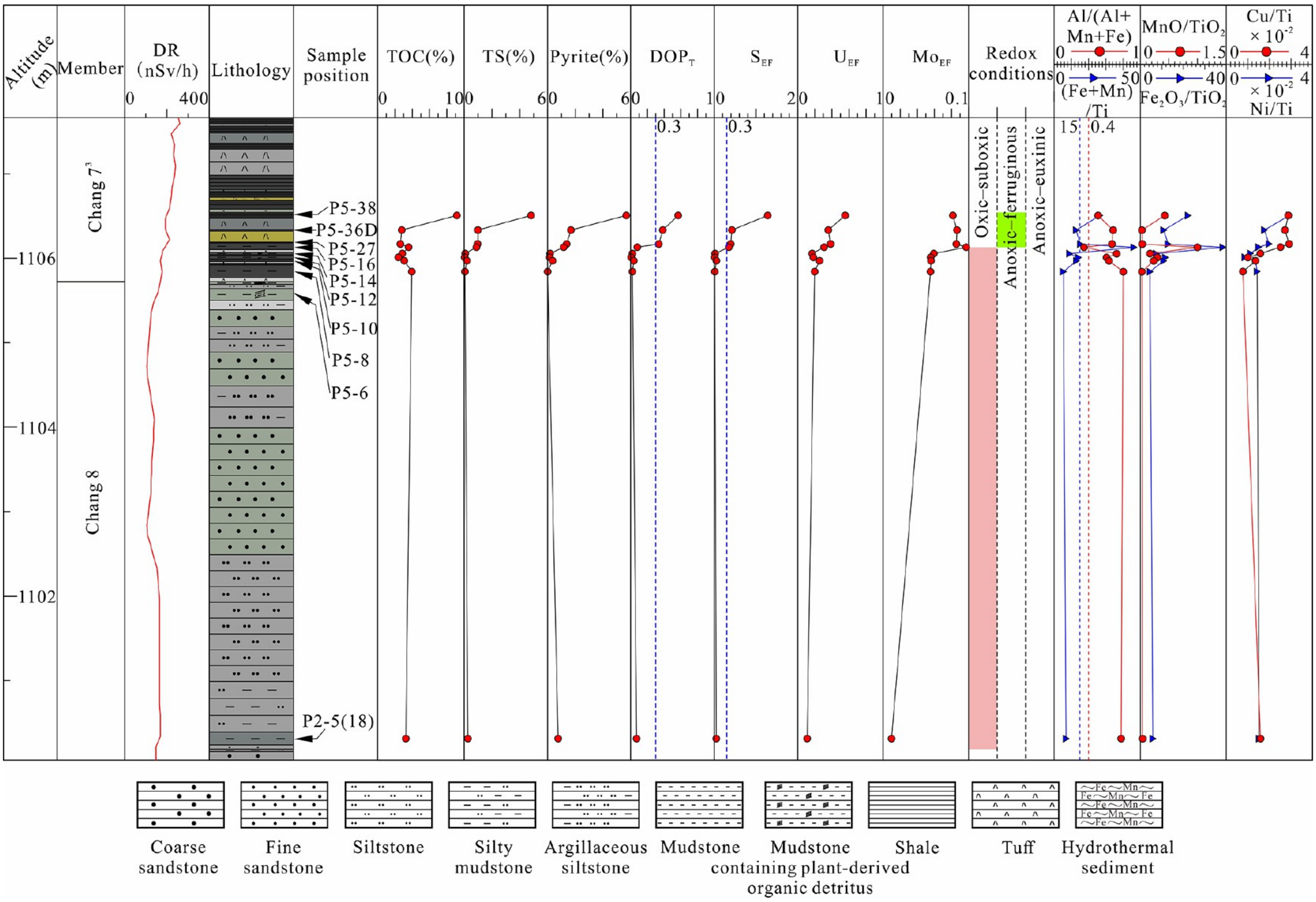

Figure 9. Redox, paleoproductivity and hydrothermal proxy profile of the Chang 8−Chang 7 Members of Motiangou outcrop in the Tongchuan district. The radioactivity of the strata was tested using an RS 230 handheld gamma spectrometer.

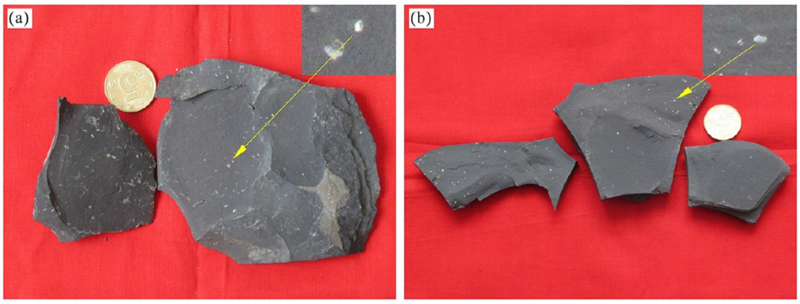

Figure 10. Calcareous ostracod fossils in samples from the layers (a) no. P5-12 and (b) no. P5-14. The white oval spot (a) and kidney shape (b) pointed by the arrows in (a) and (b) and other similar white spots are calcareous ostracod fossils, some of which are not entirely preserved.

Consistent with the absence of benthic ostracod fossils and intense hydrothermal activity in the mudstone layer no. P5-16, the S$_{EF}$ of the mudstone layer increased dramatically from 0.019 (no. P5-14) to 0.350 (no. P5-16) (Figures 7 and 9), and the change in other redox proxies is identical to that of S$_{EF}$. This synchronized transition between redox proxies and hydrothermal proxies also occurs before and after the position in the mudstone layers at the bottom of the Chang 7^3 sub-Member in Well B1, where both the DOP$_T$ and S$_{EF}$ are 0.3 (Figure 11). Accordingly, all DOP$_T$ and S$_{EF}$ corresponding to R-T(Re) (T1) in the Chang 7−Chang 8 Members of the southern Ordos Basin are 0.3.

5.1.2. Thresholds of Enrichment Degree between Anoxic−Ferruginous and Anoxic−Euxinic Conditions. In contrast to the threshold of anoxic−ferruginous conditions, the threshold of anoxic−euxinic conditions was calibrated using an organic matter-controlled enrichment degree and occurrence state model. There is just one coefficient difference between the concentration (X/Al) and enrichment factor, according to the enrichment calculation formula (X_{EF}).[14,17] Hence, our study replaced the RSE concentration (X/Al) with the enrichment factor (X_{EF}). Due to the scavenging of Mo by S-rich organic matter and formation of authigenic phases under various anoxic conditions,[33,82,83] the Mo$_{EF}$ of fine-grained sedimentary rocks exhibits distinct correlations with TOC under various redox conditions. The Mo$_{EF}$ of fine-grained sedimentary rocks with S$_{EF}$ < 0.3 is relatively low, ranging from 0.010 to 0.071 for TOC values between 0.25 and 5.70%. It exhibits an

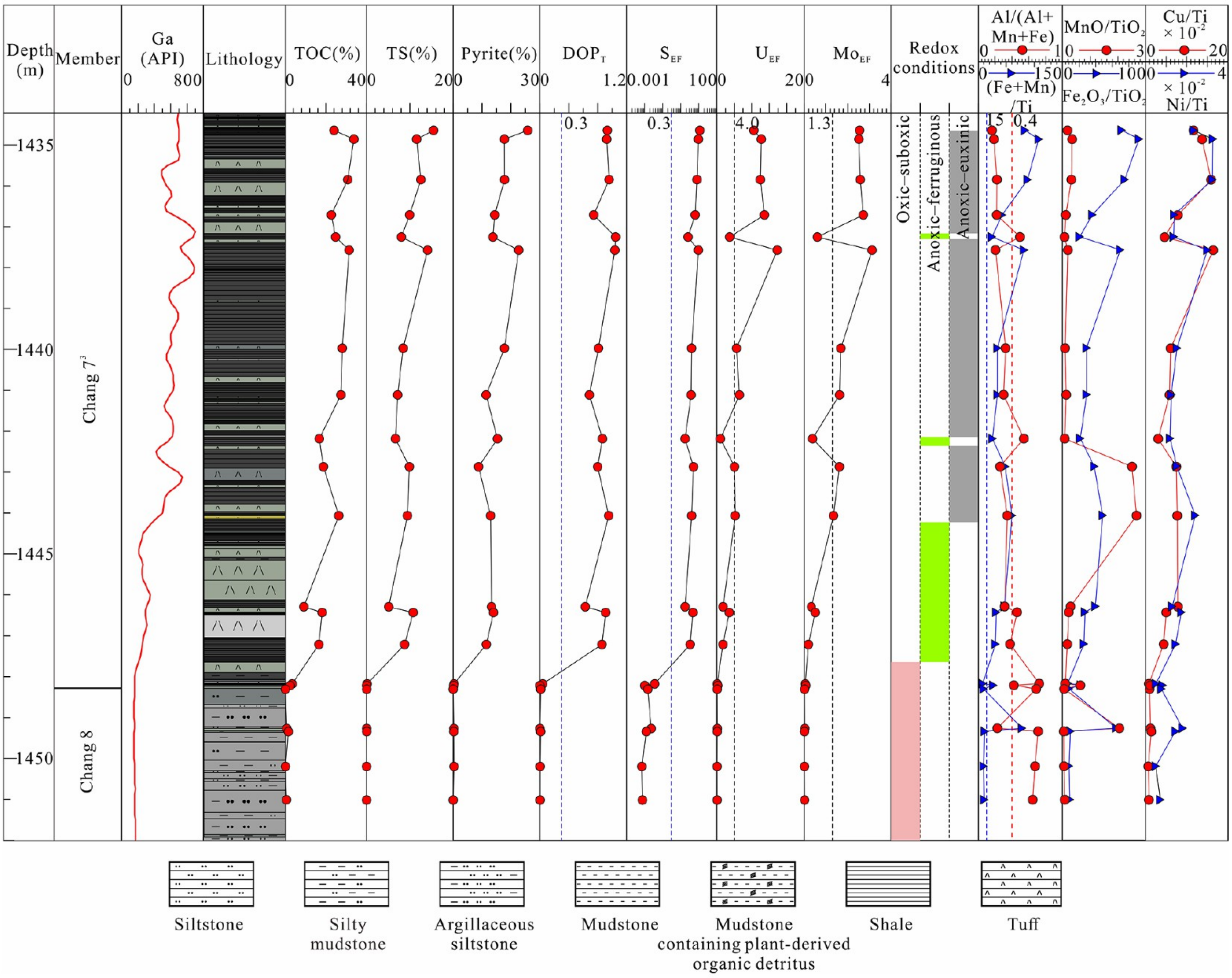

Figure 11. The redox, paleoproductivity and hydrothermal proxy profile of the Chang 8–Chang 7 Members of Well B 1 in the Jinghe district.

uncorrelated pattern with increasing TOC (Figure 12a), indicating oxic–suboxic (suboxidized) conditions in the bottom water,[18] which is compatible with evaluation outcomes based on the enrichment sequence of RSEs (Figures 4 and 6). Within the TOC range of 2.63–26.36%, the Mo_{EF} of fine-grained sedimentary rocks with $S_{EF} > 0.30$ and Mo_{EF} from 0.034 to 0.803 increases linearly with TOC, showing that these rocks were deposited under anoxic–ferruginous conditions (Figure 12a). The remaining fine-grained sedimentary rocks with Mo_{EF} = 1.352–3.124 exhibit a weak covariation or an uncorrelated distribution with TOC rise within the TOC range of 18.87–33.84% (Figure 12a), indicating deposition under anoxic–euxinic conditions. These fine-grained sedimentary rocks are Chang 7^3 sub-Member shales with Fe_2O_{3EF}, S_{EF}, and Mo_{EF} values >1.0 (Table S3). This suggests that the H_2S content of the bottom water during the deposition of these shale deposits may have been higher than that of the anoxic–euxinic organic-rich Black Sea sediments.

As a result of the co-enrichment of U and Mo (Figure 3f), the U_{EF}–TOC correlation diagram displays a similar pattern to the Mo_{EF}–TOC correlation diagram (Figure 12a,b). The U_{EF} values for oxic–suboxic (suboxidized), anoxic–ferruginous, and anoxic–euxinic conditions are 0.074–0.285, 0.125–2.965, and 4.054–13.830, respectively (Figure 12b). Despite the positive correlation between U_{EF} and TOC in anoxic–ferruginous conditions, organic matter may not be the primary host phase for U. Positive correlation between U_{EF} and TOC may represent the influence of reactive organic matter on microbially mediated U(V) reduction.[40] In addition, electron microprobe analysis, α-fission track, and sequential extraction studies revealed that a small amount of U is adsorbed onto the organic matter in the Chang 7 Member of the Ordos Basin shale.[36] The V_{EF}–TOC interactions throughout various TOC ranges likewise exhibit the diverse redox patterns proposed by Algeo and Maynard (2004)[18] (Figure 12c). Under anoxic–ferruginous conditions, the V_{EF} of samples with TOC between 2.63 and 26.36% is positively correlated with TOC (Figure 12c). Under mildly reducing circumstances, it may involve removing V(IV) ionic species by forming organometallic ligands such as V-porphyrin.[84,85] Therefore, there is a bit of overlap of V_{EF} between anoxic–ferruginous and anoxic–euxinic conditions (Figure 12c). Because the enrichment of Re appears to be solely related to the reducing extent of bottom water,[74] the correlation between Re_{EF} and TOC is irrelevant under different redox conditions (Figure 12d).

Due to the overlap between nearby redox conditions (Figure 12a–c), the TOC thresholds established by Algeo and Maynard (2004)[18] cannot be used to successfully differentiate between distinct redox conditions, even in the cases given by Algeo and Maynard (2004).[18] However, under anoxic–euxinic

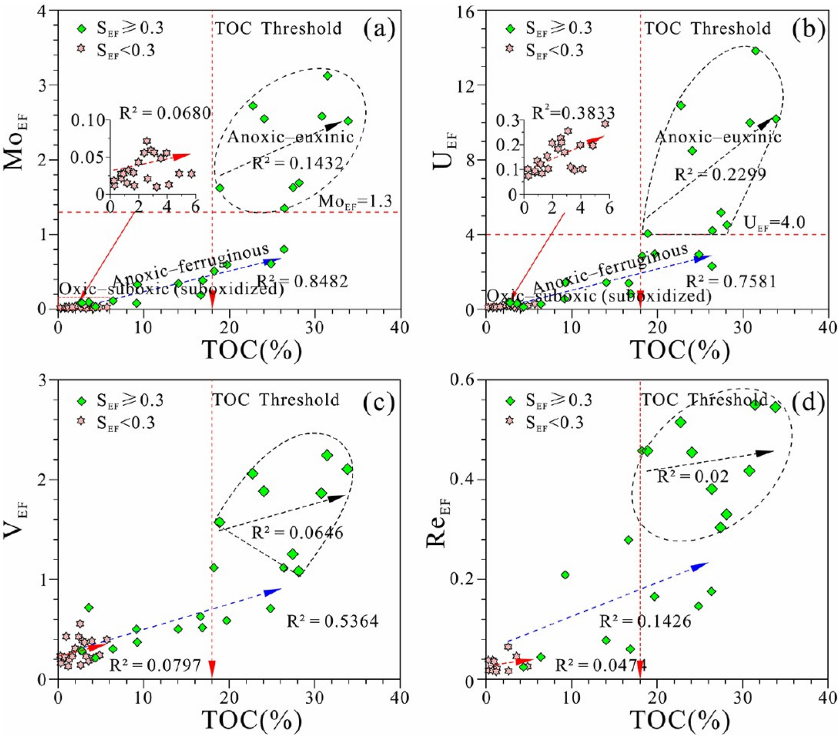

Figure 12. (a–d) Cross plots of TOC–Mo_{EF}–U_{EF}–V_{EF}–Re_{EF} of fine-grained sedimentary rocks from the Chang 8–Chang 7 Members in the southern Ordos Basin. The larger symbols in (c) and (d) are the samples with Mo_{EF} > 1.3 and U_{EF} > 4.0.

conditions, the Mo_{EF} and U_{EF} of fine-grained sedimentary rocks are above 1.3 and 4.0, respectively, which are considerably greater than those under anoxic–ferruginous conditions. Therefore, the RSE enrichment threshold (E-T) was utilized to differentiate between anoxic–euxinic and anoxic–ferruginous conditions. E-T represents the degree of RSE enrichment at the onset of various redox conditions. In accordance with this, the Mo_{EF} and U_{EF} corresponding to E-T(Mo) and E-T(U) of anoxic–euxinic conditions in the Chang 8–Chang 7 Members are 1.3 and 4.0, respectively (Figures 12a,b and 13). Mo and U are more abundant in the anoxic–euxinic shale of the Chang 7^3 sub-Member than in the anoxic–euxinic organic-rich sediments of the Black Sea (Figure 12a,b).

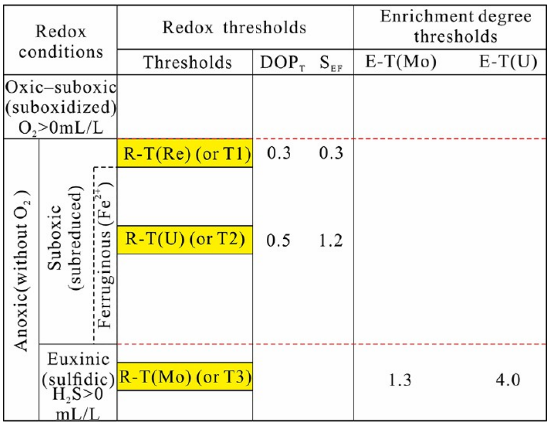

Redox conditions			Redox thresholds			Enrichment degree thresholds	
			Thresholds	DOP_T	S_{EF}	E-T(Mo)	E-T(U)
Oxic–suboxic (suboxidized) O_2>0mL/L							
Anoxic(without O_2)	Suboxic (subreduced)	Ferruginous (Fe^{2+})	R-T(Re) (or T1)	0.3	0.3		
			R-T(U) (or T2)	0.5	1.2		
	Euxinic (sulfidic) H_2S>0 mL/L		R-T(Mo) (or T3)			1.3	4.0

Figure 13. Redox thresholds and enrichment degree thresholds of different redox conditions of the Chang 8–Chang 7 Members in the southern Ordos Basin.

DOP_T of Chang 8–Chang 7 fine-grained sedimentary rocks increases with the pyrite content and approaches 1.0 (Figure 5b), whereas the Fe_{mol}/S_{mol} ratio decreases with the pyrite content and approaches the atomic molar ratio of Fe and S in pyrite (Fe_{mol}/S_{mol} = 0.5) (Figure 5c). Consequently, pyrite can serve as a redox proxy. In addition to containing organic material, pyrite also contains Mo[34,75,86] and U.[36] The distinct redox patterns are also visible in the compound covariation between the pyrite content and Mo_{EF} or U_{EF} (Figure 14a,b). The pyrite content corresponds to oxic–suboxic, anoxic–ferruginous, and anoxic–euxinic conditions within 0–2.14%, 1.16–21.72%, and 8.79–25.81%, respectively (Figure 14a,b). Because V is not trapped in Fe-sulfides,[18] V_{EF} is not linked with the pyrite content under anoxic–ferruginous conditions (Figure 14c). Likewise, Re_{EF} is not correlated with the pyrite content under anoxic–ferruginous conditions (Figure 14d), as the enrichment of Re appears to be only controlled by reducing conditions.[74]

The uncorrelated, positive, and weakly positive correlations between Mo_{EF} (or U_{EF}) and TOC (or pyrite content) are also observed in the Mo_{EF} (or U_{EF})–DOP_T (or S_{EF}) correlation diagrams (Figures 4c,d and 6c,d). The DOP_T and S are positive for pyrite (Figure 5a,b), a key electron reservoir and host phase for U and Mo. This indicates that the correlation between Mo_{EF} (or U_{EF}) and DOP_T (or S_{EF}) includes the sequence model controlled by the redox potential and enrichment degree and occurrence state model controlled by organic matter. Therefore, it is recommended to use the correlation between DOP_T (or S_{EF}) and Mo_{EF} (or U_{EF}) to calibrate the redox and enrichment degree thresholds (Figures 4c,d and 6c,d). In addition, the overlap of DOP_T and S_{EF} between anoxic–ferruginous and anoxic–euxinic conditions shows that DOP_T and S_{EF} should be applied in conjunction with redox patterns (Figures 4c,d and 6c,d).

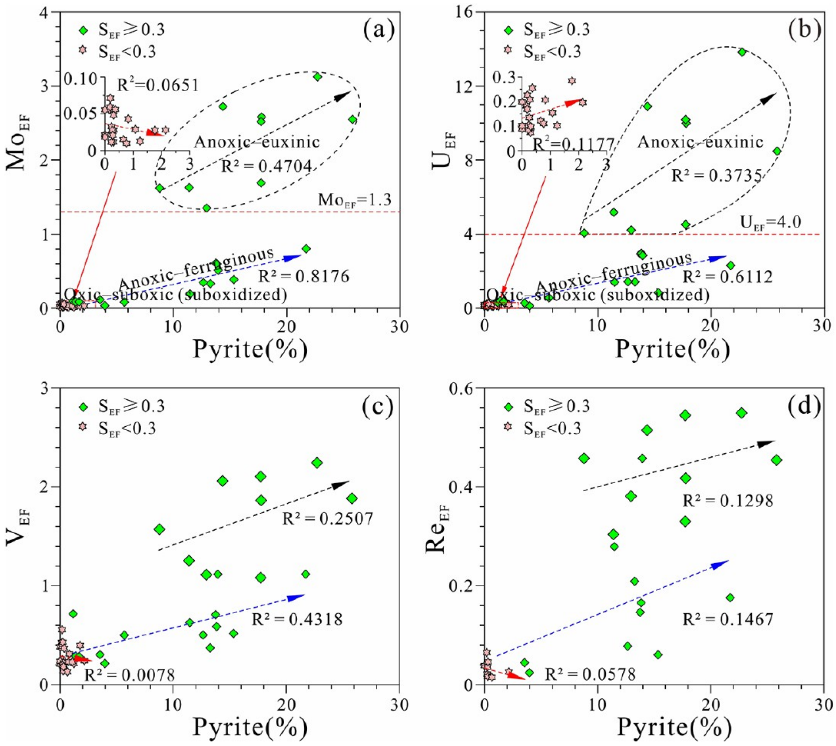

Figure 14. (a–d) Cross plots of pyrite content–Mo_{EF}–U_{EF}–V_{EF}–Re_{EF} of fine-grained sedimentary rocks from the Chang 8–Chang 7 Members in the southern Ordos Basin. The larger symbols in (c) and (d) are the samples with $Mo_{EF} > 1.3$ and $U_{EF} > 4.0$.

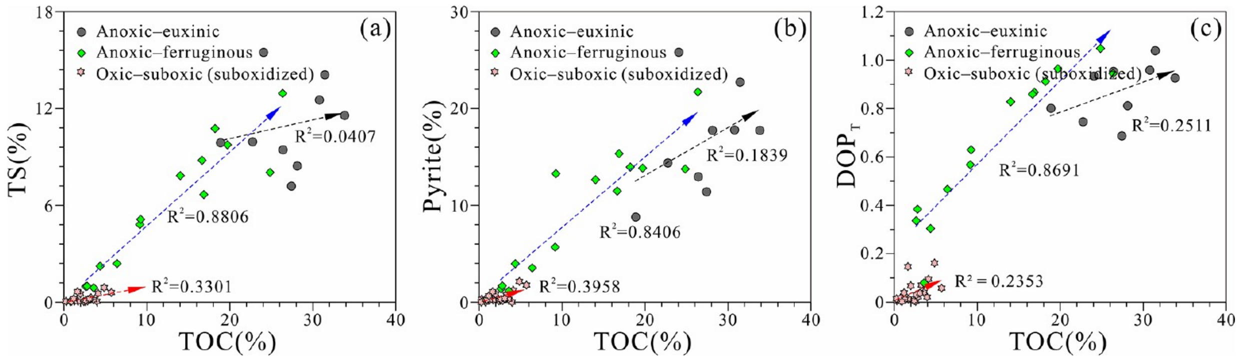

Figure 15. Cross plots of (a) TOC–TS, (b) TOC–pyrite, and (c) TOC–DOP_T of fine-grained sedimentary rocks from the Chang 8–Chang 7 Members.

Distinct correlations between TOC–TS, TOC–pyrite content, and TOC–DOP_T indicate that the enrichment degree and occurrence states of U and Mo are controlled by organic matter during different sedimentary periods in anoxic–ferruginous and anoxic–euxinic settings (Figure 15a–c). H_2S comes from bacterial sulfate reduction of sedimentary organic matter,[87] resulting in its concentration being controlled by TOC.[88] Under anoxic–ferruginous conditions, as the H_2S for synthesis of pyrite is from the bacterial sulfate reduction of syn-sedimentary organic matter only below the SWI,[89] the diagenetic pyrite content is controlled by syn-sedimentary organic matter.[89] It produces a positive correlation between TOC–TS, TOC–pyrite content, and TOC–DOP_T (Figure 15). Because the pyrite and syn-sedimentary organic matter is the host for U or Mo[36,75] and H_2S is also involved in the authigenic enrichment process of U and Mo,[33,73] their content or associated proxies are positively correlated with U_{EF} and Mo_{EF} (Figures 4c,d, 6c,d, and 14a,b).

However, under anoxic–euxinic conditions, $H_2S(aq)$ in bottom water originates mostly from the bacterial sulfide reduction of pre-sedimentary organic matter as opposed to syn-sedimentary organic matter. In H_2S-rich bottom water, an abundance of pyrite forms in the upper sulfidic column[90−93] and deposits with syn-sedimentary organic debris. The content of these pyrites is mostly determined by the availability of Fe^{2+}.[93−95] This results in a weak correlation of TOC–TS, TOC–pyrite concentration, and TOC–DOP_T under anoxic–euxinic conditions (Figure 15a–c). In addition to the U and Mo sequestered in the syn-sedimentary pyrite or organic matter, a multitude of authigenic U and Mo formed via reduction reaction is often deposited with syn-sedimentary organic matter in the surface layers.[18] The co-enrichment of Mo (or U) with different occurrence states with organic matter (or pyrite) induces a much higher Mo_{EF} (or U_{EF}) and a weakly positive relationship between Mo_{EF} (or U_{EF}) and TOC (or

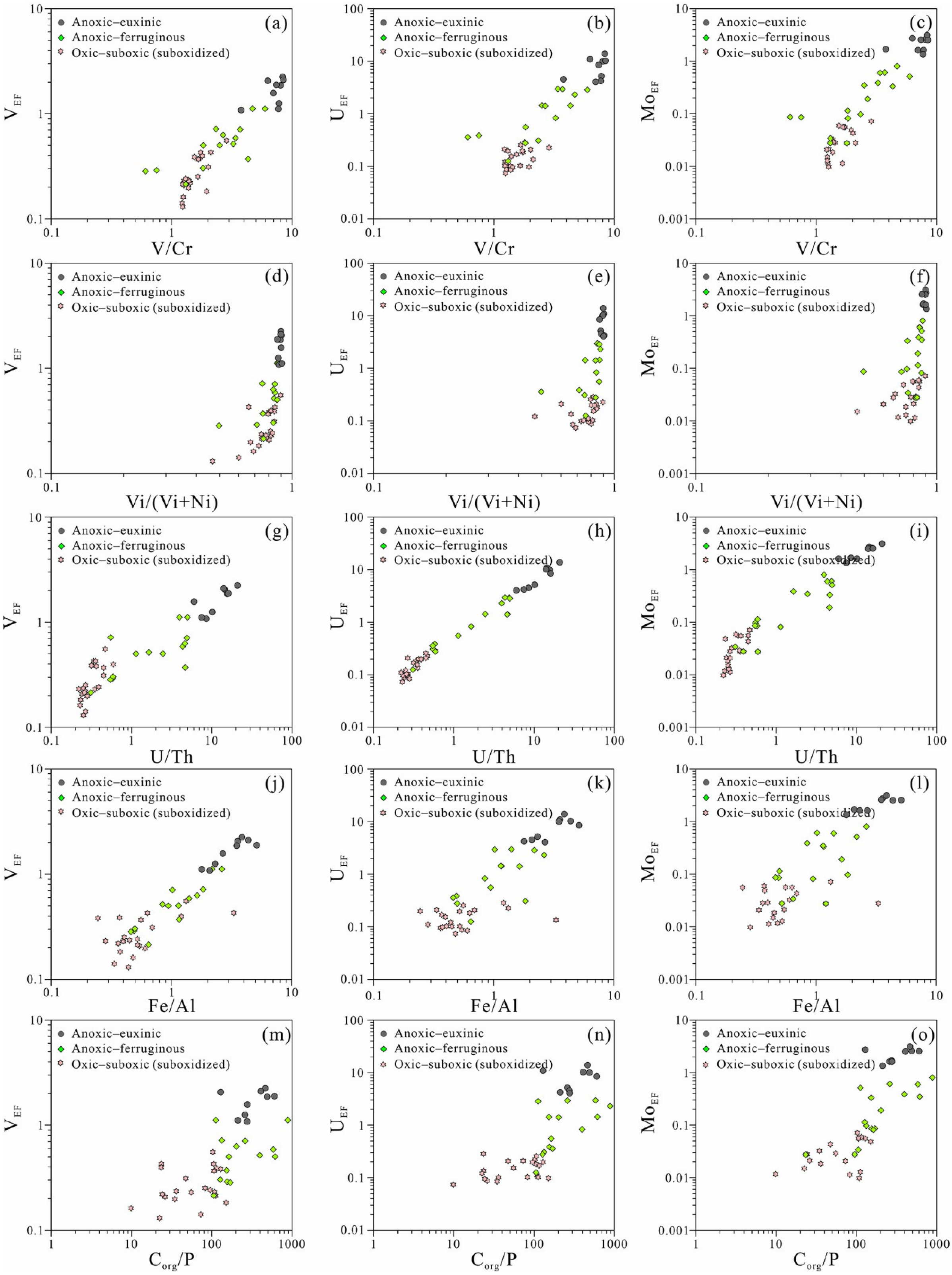

Figure 16. (a–o) Cross plots of V_{EF}, U_{EF} and Mo_{EF} versus V/Cr, Vi/(Vi + Ni), U/Th, Fe/Al, and C_{org}/P of fine-grained sedimentary rocks in Chang 8–Chang 7 Members.

pyrite content) under anoxic–euxinic conditions (Figures 12a,b and 14a,b).

5.1.3. Calibration of Earlier Redox Proxies. V/Cr,[22,29,30,53,96−102] V/(V + Ni) (or V/Ni),[26,30,97,100,103−105] U/Th (or δU, Th/U),[26,27,29,53,96,97,99,101−103] Fe/Al,[101] and C_{org}/P[25,28,98,106] with specific threshold values were used as redox proxies in previous studies on redox conditions of the Chang 7 Member. However, V/Cr, V/(V + Ni), U/Th, and

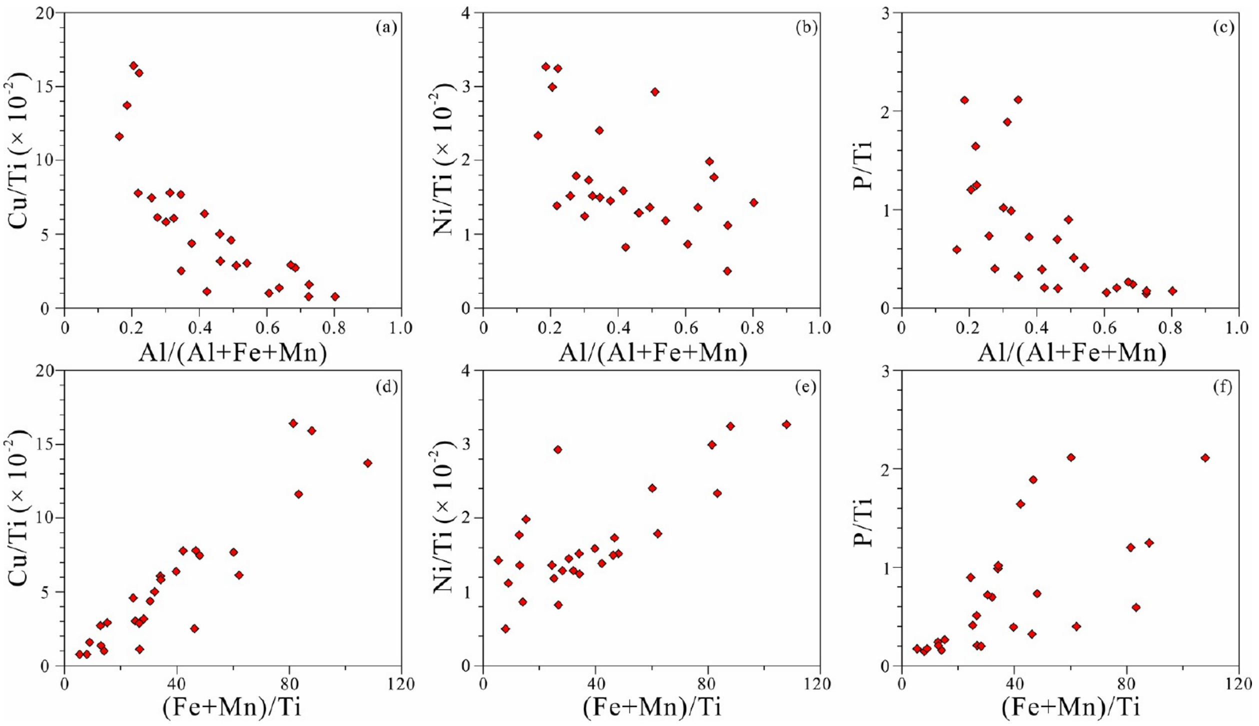

Figure 17. (a−f) Cross plots of Al/(Al + Fe + Mn)−Cu/Ti−Ni/Ti−P/Ti and (Fe + Mn)/Ti−Cu/Ti−Ni/Ti−P/Ti of fine-grained sedimentary rocks from the Chang 7^3 sub-Member of Well B1 and Motiangou outcrop in the southern Ordos Basin.

Fe/Al (Fe_2O_3/Al_2O_3) are generally positively correlated with V_{EF}, U_{EF}, and Mo_{EF}, and no compound covariation patterns exist between these redox proxies and enrichment factors except C_{org}/P (Figure 16a−l). In addition, the oxic−suboxic (suboxidized) and anoxic−ferruginous ranges of these redox proxies overlap. This shows that these redox proxies cannot be utilized to identify the enrichment sequence of RSEs and calibrate thresholds between various redox conditions. Although there is compound covariation between C_{org}/P and RSE enrichment factors (V_{EF}, U_{EF}, and Mo_{EF}) (Figure 16m−o), the overlap of C_{org}/P between the oxic−suboxic (suboxidized) and anoxic means that it cannot be used as a reliable redox proxy to identify the threshold between them. Therefore, it is not suggested to utilize these redox proxies to evaluate redox conditions in the Chang 8−Chang 7 Members of the Ordos Basin.

5.2. Evolution and Affecting Factors of Redox Conditions of Bottom Water. Based on these calibrated thresholds (Figure 13) and the variation of S_{EF}, DOP_T, U_{EF}, and Mo_{EF} from the Chang 8 Member to Chang 7^3 sub-Member in the Jinghe and Tongchuan districts (Figures 9 and 11), an entire redox evolution sequence including oxic−suboxic (suboxidized), anoxic−ferruginous, and anoxic−euxinic conditions develops in this unit, which is consistent with the increase in paleolake water depth and area increase from the Chang 8 Member to Chang 7^3 sub-Member. From the mudstone layer of the Chang 8 Member to that of the Chang 7^3 sub-Member, oxic−suboxic (suboxidized) conditions emerge prior to the severe hydrothermal activity indicated by Period-I carbonatite (Figures 7a and 9). After Period-I carbonatite, S_{EF}, U_{EF}, and Mo_{EF} rise dramatically and anoxic−ferruginous conditions occur from the thin mudstone layer no. P5-16 to the base of the shale layer of the Chang 7^3 sub-Member (Figure 9). After a particular thickness of shale was deposited under anoxic−ferruginous conditions, anoxic−euxinic conditions accompanied by sporadic anoxic−ferruginous conditions evolved in the shale layer of the Chang 7^3 sub-Member (Figure 11). Therefore, there is a positive evolution sequence of redox conditions in the Chang 7^3 sub-Member of the southern Ordos Basin deep-lake environment.

The fluctuation of Al/(Al + Fe + Mn) (<0.4, indicating hydrothermal sediment)[52,64,65] and (Fe + Mn)/Ti (>15, indicating hydrothermal sediment)[52,64,65] of the mudstone and shale in Well B1 and Motiangou field suggests sustained hydrothermal activity in the deep-lake environment of the southern Ordos Basin (Figures 9 and 11). The hydrothermal proxy curves in the profile of the Motiangou outcrop in the Tongchuan district and Well B1 in the Jinghe district exhibit nearly synchronous variation with the redox conditions (Figures 9 and 11). Hydrothermal activity appears to control the formation of anoxic conditions, based on the synchronicity between the redox and hydrothermal proxies (Figures 9 and 11). Enhanced hydrothermal activity allowed the development of anoxic−ferruginous conditions in a thin mudstone section at the base of Chang 7^3 sub-Member (Figures 9 and 11). In contrast, the dramatic weakening of hydrothermal activity in Well B1 considerably decreased the extent of reduction in the anoxic−euxinic sections (Figure 11). However, intense hydrothermal activity in the mudstone layer no. P5-16 in the Motiangou profile and the shale at the bottom of the shale sections in Well B1 only produced anoxic−ferruginous conditions (Figures 9 and 11). It suggests that hydrothermal activity hastens the emergence of anoxic−ferruginous conditions but cannot directly produce anoxic−euxinic conditions in the Chang 7^3 sub-Member (Figure 9).

The paleoproductivity proxies Cu/Ti and Ni/Ti of the anoxic−euxinic sections in the Chang 7^3 Member of Well B1 are 5.82×10^{-2}−16.41×10^{-2} (average: 10.28×10^{-2}) and 1.24×10^{-2}−3.27×10^{-2} (average: 2.21×10^{-2}) (Figure 11), respectively. Cu/Ti and Ni/Ti of the anoxic−ferruginous

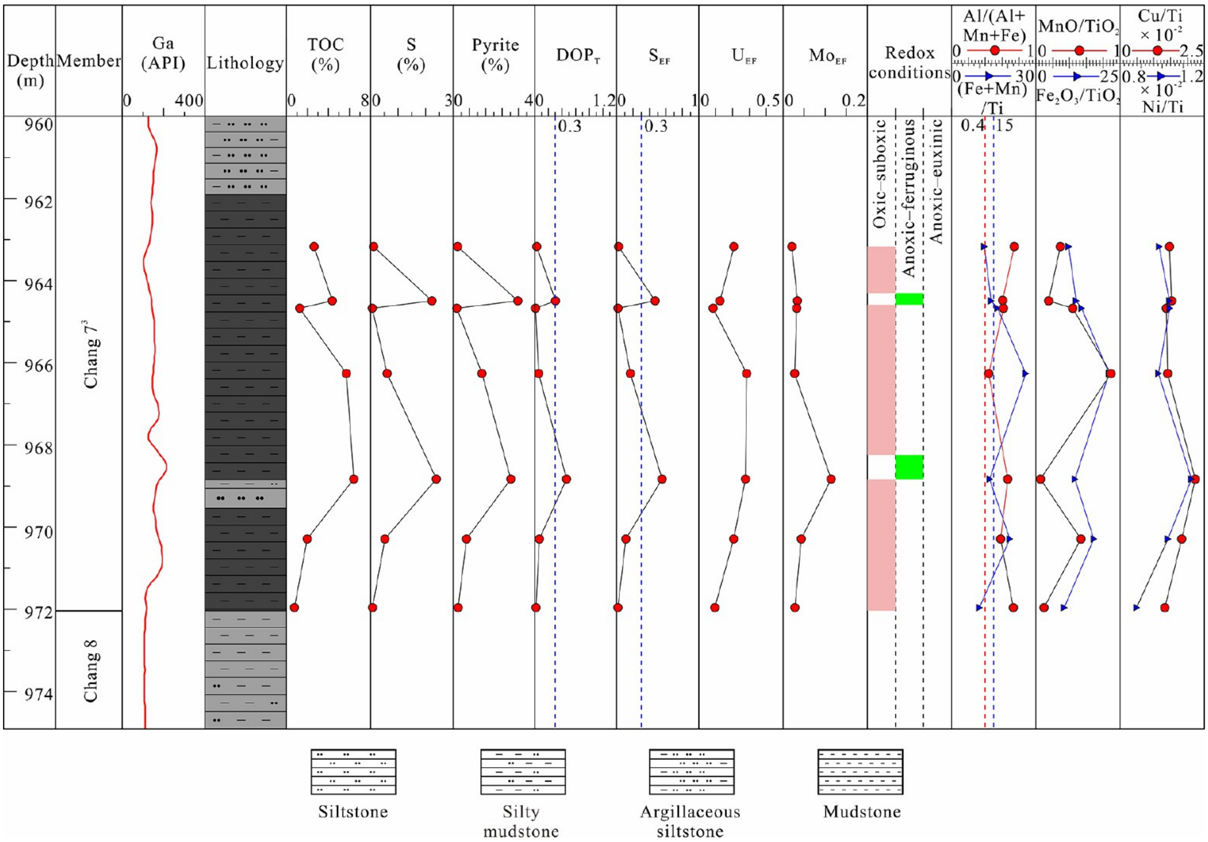

Figure 18. Redox, paleoproductivity and hydrothermal proxy profile of Chang 7^3 sub-Member of Well LH 2 in the Luohe district.

sections in the Chang 7^3 Member of Well B1 are 4.37×10^{-2}–7.80×10^{-2} (average: 5.73×10^{-2}) and 1.29×10^{-2}–1.73×10^{-2} (average: 1.49×10^{-2}), respectively. This suggests that high paleoproductivity was always sustained from the formation of the anoxic sections in Chang 7^3 sub-Member. The phosphate nodule and fossils in Chang 7 Member were often been reported.[28,107] In addition, P in sediments is solubilized and partly returned to the bottom water in the reducing environment.[21,108,109] Therefore, although the variation trend of P/Ti is similar to that of Cu/Ti and Ni/Ti in Chang 7–Chang 8 Members of Jinghe and Luohe districts, it is adopted as an aided paleoproductivity proxy and not discussed in detail here. Its data are listed in Table S4.

The variation trend of TOC in the profile is the same as that of paleoproductivity proxies (Figure 11), which show that paleoproductivity regulated the enrichment of organic matter. Although the variation of Cu/Ti and Ni/Ti indicates a slight decrease in paleoproductivity from the bottom to the top of the anoxic–euxinic sections, the TOC of the anoxic–euxinic sections (18.87–33.84%) is generally greater than that of the anoxic–ferruginous sections (9.25–18.21%) (Figure 11). This may be related to the decrease in dilution of terrigenous and volcanic detrital material, which can arise from increasing water depth[110] and the diminished strength of volcanic eruption represented by the thickness fluctuation of the tuff in Well B1 (Figure 11).

Moreover, based on isotopic analysis of sedimentary pyrite, the S of organic-rich fine-grained rocks in the Chang 7 Member is thought to have originated from atmospheric precipitation or surface runoff rather than hydrothermal processes.[98] This shows that the H_2S in anoxic–euxinic conditions largely arises from the bacterial sulfate reduction of organic matter, although it can also be observed in hydrothermal vents.[80] In addition, anoxic–euxinic conditions emerge following the maximum of Cu/Ti and Ni/Ti in anoxic–ferruginous conditions and a particular thickness of high-abundance organic matter sections (Figure 11). Consequently, the formation of anoxic–euxinic conditions in the Chang 7 Member is predicated on the maintenance of high production.

The necessary TOC threshold for forming anoxic–euxinic conditions in the Chang 7^3 sub-Member is 18% (Figure 12), which is considerably greater than that of the Black Sea sediments (strongly restricted basin, TOC at 0.5%) and Saanich Inlet sediments (weakly restricted basin, TOC > 3%).[15,111] This also shows that lacustrine basins with substantial terrestrial inputs must maintain high paleoproductivity for forming anoxic–euxinic conditions.

Similar to correlations between hydrothermal proxies and redox proxies, the hydrothermal proxies are also roughly synchronous with paleoproductivity proxies in the Chang 7^3 sub-Member in the Motiangou profile and Well B1 (Figures 9, 11 and 17). This synchronous relationship indicates that enhanced hydrothermal activity increased paleoproductivity, whereas hypoactive hydrothermal activity reduced paleoproductivity. In the deep lacustrine environment, the release and movement of common nutritional elements such as Fe, Mn, Zn, Cu, NH_4^+, NO_3^-, and PO_4^{3-}[80] to the surface water increased planktonic algae production. These nutrient materials may also enhance the chemosynthesis of photosynthetic bacteria in the anoxic–euxinic zone of the water column, which was observed in the shallow marine hydrothermal vent.[112−114] PO_4^{3-} from hydrothermal fluid compensated for the low supply of PO_4^{3-} from volcanic material in the anoxic−euxinic region in the Chang 7^3 sub-Member owing to its poor mobility during the weathering of ash.[115] Sustained supply of nutrient material via hydrothermal activity, particularly PO_4^{3-}, along with nutrient material from volcanic ash, particularly Fe,[116,117] fostered sustained blooming of algae in the anoxic−euxinic sections. Continuous algal bloom provided huge amounts of organic matter for the bacterial sulfate reaction and maintained the development of anoxic−euxinic conditions. The abnormal hydrothermal and paleoproductivity proxy values in the Chang 8 Members of Well B1 (mudstone layer no. B1-287-1 with abundant plant detritus) (Figure 11, Table S4) may be caused by the formation of siderite (20.58%) (Table S2) and its isomorphic rhodochrosite during the diagenesis under the shore-shallow lacustrine environment.

Variation in S_{EF} (or DOP_T) and Mo_{EF} (or U_{EF}) in the silt-bearing mudstone section of the Chang 7^3 sub-Member in Well LH 2 indicates that the mudstone section in the Chang 7^3 sub-Member in the Luohe district was primarily deposited under oxic−suboxic (suboxidized) conditions and intermittent anoxic−ferruginous conditions (Figure 18). This is compatible with the unstable hydrodynamic conditions in the semi-deep lake adjacent to the delta environment,[45] which can be indicated by the frequent occurrence of micron-scale silty laminae interbedded with argillaceous laminae in the mudstone section.

Besides the hydrothermal proxies in the mudstone section of the Chang 7^3 sub-Member in Well LH 2, the redox proxy curves exhibit a pattern similar to those of paleoproductivity and TOC (Figure 18). Cu/Ti (or TOC) of the anoxic−ferruginous conditions corresponds to the relatively low (Fe + Mn)/Ti or high Al/(Al + Fe + Mn) values (Figure 18). This suggests that high paleoproductivity is advantageous for developing anoxic−ferruginous conditions in the Chang 7^3 sub-Member of the Luohe district. Weakened hydrothermal activity is more favorable for raising paleoproductivity and developing anoxic−ferruginous conditions (Figure 18). In a semi-deep lacustrine setting, unstable hydrodynamic circumstances and insufficient water depth may permit hydrothermal fluid to upwell straight to the surface water, resulting in decreased paleoproductivity in the surface water. However, the hydrothermal fluid itself may be harmful to lacustrine algae on the surface water if it has a high concentration of reducing material, although it can provide nutritious material such as NH_4^+, NO_3^-, and PO_4^{3-}.[80] This suggests that hydrothermal activity is not necessarily conducive to paleoproductivity. Therefore, the anoxic−ferruginous environment in a semi-deep lacustrine setting is primarily created by the consumption of dissolved O_2 during the decomposition of organic matter and is governed by paleoproductivity.

6. CONCLUSIONS

The internal cross-calibration approach of multiple proxies based on the enrichment sequence model of RSEs controlled by redox potential and enrichment degree and occurrence state model of RSEs controlled by host phases is applicable in the lacustrine strata. The cross plots of DOP_T−Mo_{EF} (or U_{EF}) and S_{EF}−Mo_{EF} (or U_{EF}) containing the double redox assessment models are recommended, which can effectively differentiate various redox conditions. To identify the precise threshold value, the geochemical profiles of the redox proxy, mineral analysis, and paleontological information are required.

DOP_T, S_{EF}, U_{EF}, and Mo_{EF} are effective redox proxies in lacustrine strata in the Ordos Basin. However, these redox proxies should be used in conjunction with redox patterns when determining the redox extent. V/Cr, V/(V + Ni) (or V/Ni), U/Th, Fe/Al, and C_{org}/P are not advised for assessing redox conditions in the lacustrine strata of the Ordos Basin. DOP_T and S_{EF} values corresponding to R-T(Re) (T1) of the Chang 7−Chang 8 Members are both at 0.3. In addition, the DOP_T and S_{EF} values corresponding to R-T(U) (T2) of the Chang 7−Chang 8 Members are 0.5 and 1.2, respectively. E-T(Mo) and E-T(U) are 1.3 and 4.0, respectively, between the anoxic−ferruginous and anoxic−euxinic conditions.

The Chang 7^3 sub-Member deep lacustrine organic-rich shale in the southern Ordos Basin was deposited predominantly under anoxic−euxinic conditions with intermittent anoxic−ferruginous conditions. The semi-deep lacustrine organic-rich mudstone in the Chang 7^3 sub-Member of the Luohe district is primarily deposited under oxic−suboxic (suboxidized) conditions with sporadic anoxic−ferruginous conditions. In the deep lacustrine environment, hydrothermal activity promotes the transition from oxic−suboxic (suboxidized) to anoxic−ferruginous conditions but inhibits the creation of anoxic−ferruginous conditions in the semi-deep lacustrine environment. By increasing paleoproductivity, hydrothermal activity favors the establishment of anoxic−euxinic environments. Sustained high paleoproductivity is the base for forming anoxic−euxinic conditions in a deep lacustrine environment.

■ ASSOCIATED CONTENT

Supporting Information

The Supporting Information is available free of charge at https://pubs.acs.org/doi/10.1021/acsearthspacechem.2c00262.

(Table S1) $S_{EF\text{-}UCC}$, $Fe_2O_{3EF\text{-}UCC}$, $Re_{EF\text{-}UCC}$, $V_{EF\text{-}UCC}$, $U_{EF\text{-}UCC}$, and $Mo_{EF\text{-}UCC}$, (Table S2) TOC, TS, and S-bearing and Fe-bearing mineral content, (Table S3) S_{EF}, Fe_2O_{3EF}, Re_{EF}, V_{EF}, U_{EF}, Mo_{EF}, DOP_T, Fe_{mol}/S_{mol}, V/Cr, V/(V + Ni), U/Th, Fe/Al, and C_{org}/P, and (Table S4) Al/(Al + Fe + Mn), (Fe + Mn)/Ti, MnO/TiO_2, Fe_2O_3/TiO_2, Cu/Ti, Ni/Ti, and P/Ti of fine-grained sedimentary rocks from Chang 8−Chang 7 Members in the southern Ordos Basin (PDF)

■ AUTHOR INFORMATION

Corresponding Author

Zhihuan Zhang − *State Key Laboratory of Petroleum Resources and Prospecting and College of Geoscience, China University of Petroleum-Beijing, Beijing 102249, China;* orcid.org/0000-0001-9224-3365; Email: zhangzh3996@vip.163.com

Authors

Huimin Zhang − *State Key Laboratory of Petroleum Resources and Prospecting and College of Geoscience, China University of Petroleum-Beijing, Beijing 102249, China*

Dongdong Xia − *Sinopec Petroleum Exploration and Production Research Institute, Beijing 100083, China*

Ruihui Zheng − *State Key Laboratory of Petroleum Resources and Prospecting and College of Geoscience, China University of Petroleum-Beijing, Beijing 102249, China*

Lei Cao − *State Key Laboratory of Petroleum Resources and Prospecting and College of Geoscience, China University of Petroleum-Beijing, Beijing 102249, China*

Qing Li − *State Key Laboratory of Petroleum Resources and Prospecting and College of Geoscience, China University of Petroleum-Beijing, Beijing 102249, China;* orcid.org/0000-0002-7223-4370

Hao Lu − *State Key Laboratory of Petroleum Resources and Prospecting and College of Geoscience, China University of Petroleum-Beijing, Beijing 102249, China*

Complete contact information is available at:
https://pubs.acs.org/10.1021/acsearthspacechem.2c00262

Notes

The authors declare no competing financial interest.

■ ACKNOWLEDGMENTS

We thank Dr. Ting Cai and Dr. Xiaofeng Li from the College of Geoscience, China University of Petroleum-Beijing, and Dr. Guo Chen from the College of Resources and Environment, Yangtze University for their suggestions during the early writing process. This work was financially supported by the National Science and Technology Major Project [grant no. 2017ZX05049006−001].

■ REFERENCES

(1) Poulton, S. W.; Canfield, D. E. Ferruginous conditions: a dominant feature of the ocean through earth's history. *Elements* **2011**, *7*, 107−112.

(2) Li, C.; Love, G. D.; Lyons, T. W.; Fike, D. A.; Sessions, A. L.; Chu, X. A stratified redox model for the ediacaran ocean. *Science* **2010**, *328*, 80−83.

(3) Anderson, T. F. Sources and mechanisms for the enrichment of highly reactive iron in euxinic black sea sediments. *Am. J. Sci.* **2004**, *304*, 203−233.

(4) Raiswell, R.; Canfield, D. E. Sources of iron for pyrite formation in marine sediments. *Am. J. Sci.* **1998**, *298*, 219−245.

(5) Wilkin, R. T.; Barnes, H. L.; Brantley, S. L. The size distribution of framboidal pyrite in modern sediments: an indicator of redox conditions. *Geochim. Cosmochim. Acta* **1996**, *60*, 3897−3912.

(6) Wignall, P. B.; Newton, R. Pyrite framboid diameter as a measure of oxygen deficiency in ancient mudrocks. *Am. J. Sci.* **1998**, *298*, 537−552.

(7) Van Cappellen, P.; Ingall, E. D. Benthic phosphorus regeneration, net primary production, and ocean anoxia: a model of the coupled marine biogeochemical cycles of carbon and phosphorus. *Paleoceanography* **1994**, *9*, 677−692.

(8) Algeo, T. J.; Ingall, E. Sedimentary c_{org}:p ratios, paleocean ventilation, and phanerozoic atmospheric po_2. *Palaeogeogr., Palaeoclimatol., Palaeoecol.* **2007**, *256*, 130−155.

(9) Jones, B.; Manning, D. A. C. Comparison of geochemical indices used for the interpretation of palaeoredox conditions in ancient mudstones. *Chem. Geol.* **1994**, *111*, 111−129.

(10) Elrick, M.; Gilleaudeau, G. J.; Romaniello, S. J.; Algeo, T. J.; Morford, J. L.; Sabbatino, M.; Goepfert, T. J.; Cleal, C.; Cascales-Miñana, B.; Chernyavskiy, P. Major early-middle devonian oceanic oxygenation linked to early land plant evolution detected using high-resolution u isotopes of marine limestones. *Earth Planet. Sci. Lett.* **2022**, *581*, No. 117410.

(11) Gilleaudeau, G. J.; Sahoo, S. K.; Ostrander, C. M.; Owens, J. D.; Poulton, S. W.; Lyons, T. W.; Anbar, A. D. Molybdenum isotope and trace metal signals in an iron-rich mesoproterozoic ocean: a snapshot from the vindhyan basin, india. *Precambrian Res.* **2020**, *343*, No. 105718.

(12) Gill, B. C.; Dahl, T. W.; Hammarlund, E. U.; Leroy, M. A.; Gordon, G. W.; Canfield, D. E.; Anbar, A. D.; Lyons, T. W. Redox dynamics of later cambrian oceans. *Palaeogeogr., Palaeoclimatol., Palaeoecol.* **2021**, *581*, No. 110623.

(13) Algeo, T. J.; Tribovillard, N. Environmental analysis of paleoceanographic systems based on molybdenum—uranium covariation. *Chem. Geol.* **2009**, *268*, 211−225.

(14) Tribovillard, N.; Algeo, T. J.; Baudin, F.; Riboulleau, A. Analysis of marine environmental conditions based onmolybdenum−uranium covariation—Applications to Mesozoic paleoceanography. *Chem. Geol.* **2012**, *324-325*, 46−58.

(15) Algeo, T. J.; Li, C. Redox classification and calibration of redox thresholds in sedimentary systems. *Geochim. Cosmochim. Acta* **2020**, *287*, 8−26.

(16) Bennett, W. W.; Canfield, D. E. Redox-sensitive trace metals as paleoredox proxies: a review and analysis of data from modern sediments. *Earth-Sci. Rev.* **2020**, *204*, No. 103175.

(17) Algeo, T. J.; Liu, J. A re-assessment of elemental proxies for paleoredox analysis. *Chem. Geol.* **2020**, *540*, No. 119549.

(18) Algeo, T. J.; Maynard, J. B. Trace-element behavior and redox facies in core shales of upper pennsylvanian kansas-type cyclothems. *Chem. Geol.* **2004**, *206*, 289−318.

(19) Canfield, D. E.; Thamdrup, B. Towards a consistent classification scheme for geochemical environments, or, why we wish the term 'suboxic' would go away. *Geobiology* **2009**, *7*, 385−392.

(20) Pan, Y.; Huang, Z.; Guo, X.; Wang, R.; Lash, G. G.; Fan, T.; Liu, W. A re-assessment and calibration of redox thresholds in the permian lucaogou formation of the malang sag, santanghu basin, northwest china. *Mar. Pet. Geol.* **2022**, *135*, No. 105406.

(21) Tribovillard, N.; Algeo, T. J.; Lyons, T.; Riboulleau, A. Trace metals as paleoredox and paleoproductivity proxies: an update. *Chem. Geol.* **2006**, *232*, 12−32.

(22) Zhang, K.; Liu, R.; Liu, Z. Sedimentary sequence evolution and organic matter accumulation characteristics of the chang 8−chang 7 members in the upper triassic yanchang formation, southwest ordos basin, central china. *J. Pet. Sci. Eng.* **2021**, *196*, No. 107751.

(23) Yang, Y.; Li, W.; Ma, L. Tectonic and stratigraphic controls of hydrocarbon systems in the ordos basin: a multicycle cratonic basin in central china. *Aapg Bull.* **2005**, *89*, 255−269.

(24) Fu, J.; Li, S.; Niu, X.; Deng, X.; Zhou, X. Geological characteristics and exploration of shale oil in chang 7 member of triassic yanchang formation, ordos basin, nw china. *Pet. Explor. Dev.* **2020**, *47*, 931−945.

(25) Liu, H.; Qiu, Z.; Zou, C.; Fu, J.; Zhang, W.; Tao, H.; Li, S.; Zhou, S.; Wang, L.; Chen, Z.-Q. Environmental changes in the middle triassic lacustrine basin (ordos, north china): implication for biotic recovery of freshwater ecosystem following the permian-triassic mass extinction. *Glob. Planet Change* **2021**, *204*, No. 103559.

(26) Qiu, X.; Liu, C.; Mao, G.; Deng, Y.; Wang, F.; Wang, J. Major, trace and platinum-group element geochemistry of the upper triassic nonmarine hot shales in the ordos basin, central china. *Appl. Geochem.* **2015**, *53*, 42−52.

(27) Wang, C.; Wang, Q.; Chen, G.; He, L.; Xu, Y.; Chen, L.; Chen, D. Petrographic and geochemical characteristics of the lacustrine black shales from the upper triassic yanchang formation of the ordos basin, china: implications for the organic matter accumulation. *Mar. Pet. Geol.* **2017**, *86*, 52−65.

(28) Yuan, W.; Liu, G.; Stebbins, A.; Xu, L.; Niu, X.; Luo, W.; Li, C. Reconstruction of redox conditions during deposition of organic-rich shales of the upper triassic yanchang formation, ordos basin, china. *Palaeogeogr., Palaeoclimatol., Palaeoecol.* **2017**, *486*, 158−170.

(29) Chen, G.; Gang, W.; Liu, Y.; Wang, N.; Jiang, C.; Sun, J. Organic matter enrichment of the late triassic yanchang formation (ordos basin, china) under dysoxic to oxic conditions: insights from pyrite framboid size distributions. *J. Asian Earth Sci.* **2019**, *170*, 106−117.

(30) He, C.; Ji, L.; Su, A.; Wu, Y.; Zhang, M.; Zhou, S.; Li, J.; Hao, L.; Ma, Y. Source-rock evaluation and depositional environment of black shales in the triassic yanchang formation, southern ordos basin, north-central china. *J. Pet. Sci. Eng.* **2019**, *173*, 899−911.

(31) Yuan, W.; Liu, G.; Bulseco, A.; Zhou, X. Iron speciation in organic-rich shales from the upper triassic yanchang formation, ordos basin, northern china: implications for depositional environment. *J. Asian Earth Sci.* **2021**, *220*, No. 104917.

(32) Huerta-Diaz, M. A.; Morse, J. W. Pyritization of trace metals in anoxic marine sediments. *Geochim. Cosmochim. Acta* **1992**, *56*, 2681−2702.

(33) Helz, G. R.; Miller, C. V.; Charnock, J. M.; Mosselmans, J. F. W.; Pattrick, R. A. D.; Garner, C. D.; Vaughan, D. J. Mechanism of molybdenum removal from the sea and its concentration in black shales: exafs evidence. *Geochim. Cosmochim. Acta* **1996**, *60*, 3631−3642.

(34) Bostick, B. C.; Fendorf, S.; Helz, G. R. Differential adsorption of molybdate and tetrathiomolybdate on pyrite (fes$_2$). *Environ. Sci. Technol.* **2003**, *37*, 285−291.

(35) Xu, N.; Christodoulatos, C.; Braida, W. Adsorption of molybdate and tetrathiomolybdate onto pyrite and goethite: effect of ph and competitive anions. *Chemosphere* **2006**, *62*, 1726.

(36) Zhang, B.*The geochemistry characteristics and the occurrence reason of the u-rich source rocks in chang7 member of yanchang formation, ordos basin*; Northwest University: Xi' an, 2011.

(37) Adelson, J. M.; Helz, G. R.; Miller, C. V. Reconstructing the rise of recent coastal anoxia; Molybdenum in chesapeake bay sediments. *Geochim. Cosmochim. Acta* **2001**, *65*, 237−252.

(38) Zheng, Y.; Anderson, R. F.; van Geen, A.; Kuwabara, J. Authigenic molybdenum formation in marine sediments: a link to pore water sulfide in the santa barbara basin. *Geochim. Cosmochim. Acta* **2000**, *64*, 4165−4178.

(39) Crusius, J.; Calvert, S.; Pedersen, T.; Sage, D. Rhenium and molybdenum enrichments in sediments as indicators of oxic, suboxic and sulfidic conditions of deposition. *Earth Planet. Sci. Lett.* **1996**, *145*, 65−78.

(40) Sundby, B.; Martinez, P.; Gobeil, C. Comparative geochemistry of cadmium, rhenium, uranium, and molybdenum in continental margin sediments. *Geochim. Cosmochim. Acta* **2004**, *68*, 2485−2493.

(41) Wang, J.; Wang, J. Low-amplitude structures and oil-gas enrichment on the yishaan slope, ordos basin. *Pet. Explor. Dev.* **2013**, *40*, 52−60.

(42) Zhang, Z. M.; Liou, J. G.; Coleman, R. G. An outline of the plate tectonics of china. *Geol. Soc. Am. Bull.* **1984**, *95*, 295−312.

(43) Yang, H.; Deng, X. Deposition of yanchang formation deep-water sandstone under the control of tectonic events in the ordos basin. *Pet. Explor. Dev.* **2013**, *40*, 549−557.

(44) Zhang, C.; Diwu, C.; Kröner, A.; Sun, Y.; Luo, J.; Li, Q.; Gou, L.; Lin, H.; Wei, X.; Zhao, J. Archean-paleoproterozoic crustal evolution of the ordos block in the north china craton: constraints from zircon u−pb geochronology and hf isotopes for gneissic granitoids of the basement. *Precambrian Res.* **2015**, *267*, 121−136.

(45) Yuan, X.; Lin, S.; Liu, Q.; Yao, J.; Wang, L.; Guo, H.; Deng, X.; Cheng, D. Lacustrine fine-grained sedimentary features and organicrich shale distribution pattern: a case study of chang 7 member of triassic yanchang formation in ordos basin, nw china. *Pet. Explor. Dev.* **2015**, *42*, 37−47.

(46) Yang, H.; Fu, J.; Liu, X.; Meng, P. Accumulation conditions and exploration and development of tight gas in the Upper Paleozoic of the Ordos Basin. *Pet. Explor. Dev.* **2012**, *39*, 315−324.

(47) Tang, X.; Zhang, J.; Wang, X.; Yu, B.; Ding, W.; Xiong, J.; Yang, Y.; Wang, L.; Yang, C. Shale characteristics in the southeastern ordos basin, china: implications for hydrocarbon accumulation conditions and the potential of continental shales. *Int. J. Coal Geol.* **2014**, *128-129*, 32−46.

(48) Zou, C.; Wang, L.; Li, Y.; Tao, S.; Hou, L. Deep-lacustrine transformation of sandy debrites into turbidites, upper triassic, central china. *Sediment. Geol.* **2012**, *265-266*, 143−155.

(49) Yang, M.; Li, L.; Zhou, J.; Qu, X.; Zhou, D. Segmentation and inversion of the hangjinqi fault zone, the northern ordos basin (north china). *J. Asian Earth Sci.* **2013**, *70-71*, 64−78.

(50) Yang, M.; Li, L.; Zhou, J.; Jia, H.; Sun, X.; Qu, X.; Zhou, D.; Gong, T.; Ding, C. Mesozoic structural evolution of the hangjinqi area in the northern ordos basin, north china. *Mar. Pet. Geol.* **2015**, *66*, 695−710.

(51) Luo, J.; Li, J.; Yang, B.; Dai, Y.; Li, B.; Han, Y.; Wang, H.; du, J. L. Provenance for the chang 6 and chang 8 member of the yanchang formation in the xifeng area and in the periphery ordos basin: evidence from petrologic geochemistry. *Sci. China, Ser. D: Earth Sci.* **2007**, *50*, 75−90.

(52) He, C.; Ji, L.; Wu, Y.; Su, A.; Zhang, M. Characteristics of hydrothermal sedimentation process in the yanchang formation, south ordos basin, china: evidence from element geochemistry. *Sediment. Geol.* **2016**, *345*, 33−41.

(53) Zhang, K.; Liu, R.; Liu, Z.; Li, B.; Han, J.; Zhao, K. Influence of volcanic and hydrothermal activity on organic matter enrichment in the upper triassic yanchang formation, southern ordos basin, central china. *Mar. Pet. Geol.* **2020**, *112*, No. 104059.

(54) Liu, F.; Zhu, X.; Li, Y.; Xu, L.; Niu, X.; Zhu, S.; Liang, X.; Xue, M.; He, J. Sedimentary characteristics and facies model of gravity flow deposits of late triassic yanchang formation in southwestern ordos basin, nw china. *Pet. Explor. Dev.* **2015**, *42*, 633−645.

(55) Chen, G.; Gang, W.; Chang, X.; Wang, N.; Zhang, P.; Cao, Q.; Xu, J. Paleoproductivity of the chang 7 unit in the ordos basin (north china) and its controlling factors. *Palaeogeogr., Palaeoclimatol., Palaeoecol.* **2020**, *551*, No. 109741.

(56) Little, S. H.; Vance, D.; Lyons, T. W.; Mcmanus, J. Controls on trace metal authigenic enrichment in reducing sediments: insights from modern oxygen-deficient settings. *Am. J. Sci.* **2015**, *315*, 77−119.

(57) Wedepohl, K. H. Environmental influences on the chemical composition of shales and clays. *Phys. Chem. Earth* **1971**, *8*, 307−333.

(58) Rudnick, R. L.; Gao, S.Composition of the continental crust. In *Treatise on Geochemistry*; Holland, H. D.; Turekian, K. K., Eds.; The Crust, Vol. 4, Part 4.1; Elsevier, 2014; pp. 1−51. DOI: 10.1016/B978-0-08-095975-7.00301-6.

(59) Lüschen, H.*Vergleichende anorganisch-geochemische untersuchungen an phanerozoischen corg-reichen sedimenten: ein beitrag zur charakterisierung ihrer fazies*; Universitat Oldenburg: Germany, 2004.

(60) van Kaam-Peters, H. M. E.; Köster, J.; van der Gaast, S. J.; Dekker, M.; de Leeuw, J. W.; Sinninghe Damsté, J. S. The effect of clay minerals on diasterane/sterane ratios. *Geochim. Cosmochim. Acta* **1998**, *62*, 2923−2929.

(61) Algeo, T. J.; Rowe, H. Paleoceanographic applications of trace-metal concentration data. *Chem. Geol.* **2012**, *324-325*, 6−18.

(62) Helz, G. R.; Adelson, J. M. Trace element profiles in sediments as proxies of dead zone history; Rhenium compared to molybdenum. *Environ. Sci. Technol.* **2013**, *47*, 1257−1264.

(63) Clarkson, M. O.; Poulton, S. W.; Guilbaud, R.; Wood, R. A. Assessing the utility of fe/al and fe-speciation to record water column redox conditions in carbonate-rich sediments. *Chem. Geol.* **2014**, *382*, 111−122.

(64) Boström, K.; Peterson, M. N. A.; Joensuu, O.; Fisher, D. E. Aluminum-poor ferromanganoan sediments on active oceanic ridges. *J. Geophys. Res.* **1969**, *74*, 3261−3270.

(65) Adachi, M.; Yamamoto, K.; Sugisaki, R. Hydrothermal chert and associated siliceous rocks from the northern pacific their geological significance as indication od ocean ridge activity. *Sediment. Geol.* **1986**, *47*, 125−148.

(66) Yamamoto, K. Geochemical characteristics and depositional environments of cherts and associated rocks in the franciscan and shimanto terranes. *Sediment. Geol.* **1987**, *52*, 65−108.

(67) Schoepfer, S. D.; Shen, J.; Wei, H.; Tyson, R. V.; Ingall, E.; Algeo, T. J. Total organic carbon, organic phosphorus, and biogenic barium fluxes as proxies for paleomarine productivity. *Earth-Sci. Rev.* **2015**, *149*, 23−52.

(68) Sen, A. K.; Filippelli, G. M.; Flores, J.-A. An application of wavelet analysis to paleoproductivity records from the southern ocean. *Comput. Geosci.* **2009**, *35*, 1445−1450.

(69) Yan, C.; Jin, Z.; Zhao, J.; Du, W.; Liu, Q. Influence of sedimentary environment on organic matter enrichment in shale: a case study of the wufeng and longmaxi formations of the sichuan basin, china. *Mar. Pet. Geol.* **2018**, *92*, 880−894.

(70) Li, C.; Chen, S.-J.; Liao, J.-B.; Hou, Y.-T.; Yu, J.; Liu, G.-L.; Xu, K.; Wu, X.-T. Geochemical characteristics of the chang 7 member in the southwestern ordos basin, china: the influence of sedimentary environment on the organic matter enrichment. *Palaeoworld* **2022**, DOI: 10.1016/j.palwor.2022.09.002.

(71) Omietimi, E. J.; Lenhardt, N.; Yang, R.; Götz, A. E.; Bumby, A. J. Sedimentary geochemistry of late cretaceous-paleocene deposits at the southwestern margin of the anambra basin (nigeria): implications for paleoenvironmental reconstructions. *Palaeogeogr., Palaeoclimatol., Palaeoecol.* **2022**, *600*, No. 111059.

(72) Fredrickson, J. K.; Zachara, J. M.; Kennedy, D. W.; Duff, M. C.; Gorby, Y. A.; Li, S. W.; Krupka, K. M. Reduction of u(vi) in goethite (α-feooh) suspensions by a dissimilatory metal-reducing bacterium. *Geochim. Cosmochim. Acta* **2000**, *64*, 3085−3098.

(73) Klinkhammer, G. P.; Palmer, M. R. Uranium in the oceans: where it goes and why. *Geochim. Cosmochim. Acta* **1991**, *55*, 1799−1806.

(74) Morford, J. L.; Emerson, S. R.; Breckel, E. J.; Kim, S. H. Diagenesis of oxyanions (v, u, re, and mo) in pore waters and sediments from a continental margin. *Geochim. Cosmochim. Acta* **2005**, *69*, 5021−5032.

(75) Phillips, R.; Xu, J. A critical review of molybdenum sequestration mechanisms under euxinic conditions: implications for the precision of molybdenum paleoredox proxies. *Earth-Sci. Rev.* **2021**, *221*, No. 103799.

(76) Jie, D.; Hu Zuowei, Y. X.; Jing, H.; Yun, L.; Yulong, W. The carbonate concretions of chang-7 and their hydrocarbon significance in southern ordos basin, china. *J. Chengdu Univ. Sci. Technol.* **2017**, *44*, 553−564.

(77) Zhu, R.; Cui, J.; Luo, Z.; Li, S.; Mao, Z.; Xi, K.; Su, L. Isotopic geochemical characteristics of two types of carbonate concretions of chang 7 member in the middle-upper triassic yanchang formation, ordos basin, central china. *Mar. Pet. Geol.* **2020**, *116*, No. 104312.

(78) Le Maitre, R. W.; Streckeisen, A.; Zanettin, B.; Le Bas, M. J.; Bonin, B.; Bateman, P.; Bellieni, G. A. D.; Efremova, S.; Keller, J.; et al.Recommendations of the international union of geological sciences subcommission on the systematics of igneous rocks. In *Igneous rocks*; Cambridge University Press, 2002.

(79) Dias, A.*Geochemistry of deep-sea hydrothermal sediments from the saldanha and lucky strik hydrothermal fields : (mid-aatlantic rridge)*; Universidade de Lisboa, 2009.

(80) Tarasov, V. G.; Gebruk, A. V.; Mironov, A. N.; Moskalev, L. I. Deep-sea and shallow-water hydrothermal vent communities: two different phenomena? *Chem. Geol.* **2005**, *224*, 5−39.

(81) Di Bella, M.; Sabatino, G.; Quartieri, S.; Ferretti, A.; Cavalazzi, B.; Barbieri, R.; Foucher, F.; Messori, F.; Italiano, F. Modern iron ooids of hydrothermal origin as a proxy for ancient deposits. *Sci. Rep.* **2019**, *9*, 7107.

(82) Helz, G. R.; Bura-Nakić, E.; Mikac, N.; Ciglenečki, I. New model for molybdenum behavior in euxinic waters. *Chem. Geol.* **2011**, *284*, 323−332.

(83) Vorlicek, T. P.; Helz, G. R.; Chappaz, A.; Vue, P.; Vezina, A.; Hunter, W. Molybdenum burial mechanism in sulfidic sediments: iron-sulfide pathway. *Acs Earth Space Chem.* **2018**, *2*, 565−576.

(84) Lewan, M. D.; Maynard, J. B. Factors controlling enrichment of vanadium and nickel in the bitumen of organic sedimentary rocks. *Geochim. Cosmochim. Acta* **1982**, *46*, 2547−2560.

(85) Emerson, S. R.; Huested, S. S. Ocean anoxia and the concentrations of molybdenum and vanadium in seawater. *Mar. Chem.* **1991**, *34*, 177−196.

(86) Freund, C.; Wishard, A.; Brenner, R.; Sobel, M.; Mizelle, J.; Kim, A.; Meyer, D. A.; Morford, J. L. The effect of a thiol-containing organic molecule on molybdenum adsorption onto pyrite. *Geochim. Cosmochim. Acta* **2016**, *174*, 222−235.

(87) Jørgensen, B. B.; Kasten, S.Sulfur Cycling and Methane Oxidation. In *Marine Geochemistry*, Second ed.; Schulz, H. D.; Zabel, M.; Springer: Berlin, Heidelberg, 2006; pp. 271−309. DOI: 10.1007/3-540-32144-6_8.

(88) Berner, R. A.; Westrich, J. T. Bioturbation and the early diagenesis of carbon and sulfur. *Am. J. Sci.* **1985**, *285*, 193−206.

(89) Raiswell, R.; Berner, R. A. Pyrite formation in euxinic and semi-euxinic sediments. *Am. J. Sci.* **1985**, *285*, 710−724.

(90) Lyons, T. W. Sulfur isotopic trends and pathways of iron sulfide formation in upper holocene sediments of the anoxic black sea. *Geochim. Cosmochim. Acta* **1997**, *61*, 3367−3382.

(91) Muramoto, J. A.; Honjo, S.; Fry, B.; Hay, B. J.; Howarth, R. W.; Cisne, J.; Sulfur, L. iron and organic carbon fluxes in the black sea: sulfur isotopic evidence for origin of sulfur fluxes. *Deep Sea Res. Part I Oceanogr. Res. Pap.* **1991**, *38*, S1151−S1187.

(92) Wilkin, R.; Arthur, M.; Dean, W. History of water-column anoxia in the black sea indicated by pyrite framboid size distributions. *Earth Planet. Sci. Lett.* **1997**, *148*, 517−525.

(93) Calvert, S. E.; Karlin, R. E. Relationships between sulphur, organic carbon, and iron in the modern sediments of the black sea. *Geochim. Cosmochim. Acta* **1991**, *55*, 2483−2490.

(94) Middelburg, J. J. Organic carbon, sulphur, and iron in recent semi-euxinic sediments of kau bay, indonesia. *Geochim. Cosmochim. Acta* **1991**, *55*, 815−828.

(95) Boesen, C.; Postma, D. Pyrite formation in anoxic environments of the baltic. *Am. J. Sci.* **1988**, *288*, 575−603.

(96) Zhang, K.; Liu, R.; Liu, Z.; Li, L. Geochemical characteristics and geological significance of humid climate events in the middle-late triassic (ladinian-carnian) of the ordos basin, central china. *Mar. Pet. Geol.* **2021**, *131*, No. 105179.

(97) Li, D.; Li, R.; Zhu, Z.; Wu, X.; Cheng, J.; Liu, F.; Zhao, B. Origin of organic matter and paleo-sedimentary environment reconstruction of the triassic oil shale in tongchuan city, southern ordos basin (china). *Fuel* **2017**, *208*, 223−235.

(98) Chen, G.; Chang, X.; Gang, W.; Wang, N.; Zhang, P.; Cao, Q.; Xu, J. Anomalous positive pyrite sulfur isotope in lacustrine black shale of the yanchang formation, ordos basin: triggered by paleoredox chemistry changes. *Mar. Pet. Geol.* **2020**, *121*, No. 104587.

(99) Liu, Q.; Li, P.; Jin, Z.; Liang, X.; Zhu, D.; Wu, X.; Meng, Q.; Liu, J.; Fu, Q.; Zhao, J. Preservation of organic matter in shale linked to bacterial sulfate reduction (bsr) and volcanic activity under marine and lacustrine depositional environments. *Mar. Pet. Geol.* **2021**, *127*, No. 104950.

(100) Yang, Y.; Liu, Y.; Zhou, D.; Jiao, X.; Cao, Q.; Meng, Z.; Zhao, M. Lithotypes, organic matter and paleoenvironment characteristics in the chang73 submember of the triassic yanchang formation, ordos basin, china: implications for organic matter accumulation and favourable target lithotype. *J. Pet. Sci. Eng.* **2022**, *216*, No. 110691.

(101) Li, Q.; Wu, S.; Xia, D.; You, X.; Zhang, H.; Lu, H. Major and trace element geochemistry of the lacustrine organic-rich shales from the upper triassic chang 7 member in the southwestern ordos basin, china; Implications for paleoenvironment and organic matter accumulation. *Mar. Pet. Geol.* **2020**, *111*, 852−867.

(102) Zhang, B.; Mao, Z.; Zhang, Z.; Yuan, Y.; Chen, X.; Shi, Y.; Liu, G.; Shao, X. Black shale formation environment and its control on shale oil enrichment in triassic chang 7 member, ordos basin, nw china. *Pet. Explor. Dev.* **2021**, *48*, 1304−1314.

(103) Fu, J.; Li, S.; Xu, L.; Niu, X. Paleo-sedimentary environmental restoration and its significance of chang 7 member of triassic yanchang formation in ordos basin, nw china. *Pet. Explor. Dev.* **2018**, *45*, 998−1008.

(104) Li, D.; Shi, Q.; Mi, N.; Xu, Y.; Wang, X.; Tao, W. The type, origin and preservation of organic matter of the fine-grain sediments in triassic yanhe profile, ordos basin, and their relation to paleoenvironment condition. *J. Pet. Sci. Eng.* **2020**, *188*, No. 106875.

(105) Yu, W.; Tian, J.; Wang, F.; Liang, Q.; Yang, T.; Kneller, B.; Liang, X. Sedimentary environment and organic matter enrichment of black mudstones from the upper triassic chang-7 member in the ordos basin, northern china. *J. Asian Earth Sci.* **2022**, *224*, No. 105009.

(106) Shi, J.; Zou, Y.-R.; Cai, Y.-L.; Zhan, Z.-W.; Sun, J.-N.; Liang, T.; Peng, P. Organic matter enrichment of the chang 7 member in the ordos basin: insights from chemometrics and element geochemistry. *Mar. Pet. Geol.* **2022**, *135*, No. 105404.

(107) Yao, M.; Sun, Z.; Meng, Q.; Li, J.; Jiang, D. Vertebrate coprolites from middle triassic chang 7 member in ordos basin, china: palaeobiological and palaeoecological implications. *Palaeogeogr., Palaeoclimatol., Palaeoecol.* **2022**, *600*, No. 111084.

(108) Lu, Y.; Jiang, S.; Lu, Y.; Xu, S.; Shu, Y.; Wang, Y. Productivity or preservation? The factors controlling the organic matter accumulation in the late katian through hirnantian wufeng organic-rich shale, south china. *Mar. Pet. Geol.* **2019**, *109*, 22−35.

(109) Ingall, E.; Jahnke, R. Evidence for enhanced phosphorus regeneration from marine sediments overlain by oxygen depleted waters. *Geochim. Cosmochim. Acta* **1994**, *58*, 2571−2575.

(110) Zhang, T.; Hu, S.; Bu, Q.; Bai, B.; Tao, S.; Chen, Y.; Pan, Z.; Lin, S.; Pang, Z.; Xu, W.; et al. Effects of lacustrine depositional sequences on organic matter enrichment in the chang 7 shale, ordos basin, china. *Mar. Pet. Geol.* **2021**, *124*, No. 104778.

(111) Algeo, T. J.; Lyons, T. W.Mo-total organic carbon covariation in modern anoxic marine environments: implications for analysis of paleoredox and paleohydrographic conditions: n/a−n/a. *Paleoceanography***2006**, *21*(), DOI: DOI: 10.1029/2004PA001112.

(112) Sorokin, Y. I.; Sorokin, P. Y.; Zakuskina, O. Y. Microplankton and its functional activity in zones of shallow hydrotherms in the western pacific. *J. Plankton Res.* **1998**, *20*, 1015−1031.

(113) Sorokin, Y. I. Microplankton and its function in a zone of shallow hydrothermal activity:the craternaya bay, kurile islands. *J. Plankton Res.* **2003**, *25*, 495−506.

(114) Tarasov, V. G.; Gebruk, A. V.; Shulkin, V. M.; Kamenev, G. M.; Fadeev, V. I.; Kosmynin, V. N.; Malakhov, V. V.; Starynin, D. A.; Obzhirov, A. I. Effect of shallow-water hydrothermal venting on the biota of matupi harbour (rabaul caldera, new britain island, papua new guinea). *Cont. Shelf Res.* **1999**, *19*, 79−116.

(115) Felitsyn, S. B.; Kirianov, V. Y. Mobility of phosphorus during the weathering of volcanic ashes. *Lithol. Miner. Resour.* **2006**, *37*, 275−278.

(116) Coale, K. H.; Johnson, K. S.; Fitzwater, S. E.; Gordon, R. M.; Tanner, S.; Chavez, F. P.; Ferioli, L.; Sakamoto, C.; Rogers, P.; Millero, F.; et al. A massive phytoplankton bloom induced by an ecosystem-scale iron fertilization experiment in the equatorial pacific ocean. *Nature* **1996**, *383*, 495−501.

(117) Boyd, P. W.; Watson, A. J.; Law, C. S.; Abraham, E. R.; Trull, T.; Murdoch, R.; Bakker, D. C. E.; Bowie, A. R.; Buesseler, K. O.; Chang, H.; et al. A mesoscale phytoplankton bloom in the polar southern ocean stimulated by iron fertilization. *Nature* **2000**, *407*, 695−702.